Ultrasonics Sonochemistry 71 (2021) 105406

Contents lists available at ScienceDirect

Ultrasonics Sonochemistry

journal homepage: www.elsevier.com/locate/ultson

The influence of semiconducting properties of passive films on the cavitation erosion resistance of a NbN nanoceramic coating

Jiang Xu [a,*], Shuang Peng [a], Zhengyang Li [b], Shuyun Jiang [c], Zong-Han Xie [d], Paul Munroe [e]

[a] Department of Material Science and Engineering, Nanjing University of Aeronautics and Astronautics, 29 Yudao Street, Nanjing 210016, PR China
[b] Institute of Mechanics, Chinese Academy of Sciences, Beijing 100190, PR China
[c] Department of Mechanical Engineering, Southeast University, 2 Si Pai Lou, Nanjing 210096, PR China
[d] School of Mechanical Engineering, University of Adelaide, SA 5005, Australia
[e] School of Materials Science and Engineering, University of New South Wales, NSW 2052, Australia

ARTICLE INFO

Keywords:
NbN nanoceramic coating
Ultrasonic cavitation erosion
Mott–schottky
First-principle
Point defect model

ABSTRACT

To alleviate the cavitation damage of metallic engineering components in hydrodynamic systems operating in marine environments, a NbN nanoceramic coating was synthesized on to a Ti-6Al-4V substrate via a double cathode glow discharge technique. The microstructure of the coating consisted of a ~13 μm thick deposition layer of a hexagonal δ′-NbN phase and a diffusion layer ~2 μm in thickness composed of face-centered cubic (fcc) B1-NaCl–structured (Ti,Nb)N. The NbN coating not only exhibited higher values of H/E and H^2/E than those measured from NbN coatings deposited by other techniques, but also possessed good adhesion to the substrate. The cavitation erosion resistance of the NbN coating in a 3.5 wt% NaCl solution was investigated using an ultrasonic cavitation-induced apparatus combined with a range of electrochemical test methods. Potentiodynamic polarization measurements demonstrated that the NbN coated specimens demonstrated both a higher corrosion potential (E_{corr}) and lower corrosion current density (i_{corr}) than the uncoated substrate. Mott-Schottky analysis, combined with the point defect model (PDM), revealed that, for a given cavitation time, the donor density (N_D) of the passive film on the NbN coating was reduced by 1 ~ 2 orders of magnitude relative to the uncoated Ti-6Al-4V, and the diffusivity of the point defects (D_0) in the passive film grown on the NbN coating was nearly one order of magnitude lower than that on the uncoated substrate. In order to better understand the experimental observations obtained from Mott-Schottky analysis and double-charge layer capacitance measurements, first-principles density-functional theory was employed to calculate the energy of vacancy formation and the adsorption energy for chloride ions for the passive films present on both the NbN coating and bare Ti-6Al-4V.

1. Introduction

Cavitation is a well-known physical phenomenon that usually arises in hydrodynamic systems when the static pressure of a fluid suddenly drops below the saturated vapor pressure at the operating temperature. The resultant cavitation bubbles are subsequently driven by the flow of fluid and then implode violently in a region where the liquid pressure exceeds vapor pressure [1]. The repetitive growth and collapse of bubbles creates impingement of fluid micro-jets or shock pressure wave in the proximity of solid surfaces, which may cause the amplitude of the cavitation impulse pressure to exceed 1GPa over short durations in the range from nanoseconds to microseconds [2]. In non-corrosive environments, such high impacts are essentially a mechanical process, analogous to action of shock loading or high-amplitude low-cycle fatigue [3]. The action of these impacts on a given material surface triggers initiation of local plastic deformation, brittle fracture and eventually material removal, leading to a significant decrease of efficiency and service lifetime of engineering components. However, in the presence of an aggressive aqueous solution, e.g. a marine environment, such components must withstand both mechanical load and electrochemical corrosion attack. The mutually reinforcing synergy between mechanical and electrochemical factors frequently generates sudden and catastrophic failure, particularly for components in marine or offshore applications [4].

As one of the most important corrosion-resistant metals, titanium alloys have been widely employed in the chemical, marine and offshore

* Corresponding author.
E-mail address: xujiang73@nuaa.edu.cn (J. Xu).

https://doi.org/10.1016/j.ultsonch.2020.105406
Received 29 April 2020; Received in revised form 20 October 2020; Accepted 9 November 2020
Available online 6 December 2020

industries, including pumps and valves as well as in pipelines [5]. Nonetheless, titanium alloys are unable to satisfy service requirements under a range of different cavitation environments [6]. Firstly, titanium alloys do not have adequate surface hardness to resist mechanical action of cavitation. Secondly, their good resistance to corrosion in different aggressive media is mainly associated with the presence of stable, adherent and tenacious passive films grown on their surfaces. However, the localized dynamic forces exerted by the collapse of bubbles may destroy these protective films, thus exposing underlying fresh surfaces to severe corrosive environments and thereby increasing the cavitation erosion rate. As cavitation erosion is a form of surface-controlled degradation, it is a process that relies heavily on surface mechanical properties, rather than on bulk properties of a material, extensive efforts have been dedicated to the development of surface modification methods to enhance component durability and reduce cost. Such surface coatings offer a feasible avenue to tailor chemical composition and hence surface properties as desired for the protection of metallic components from cavitation erosion damage. Generally, the cavitation erosion resistance of a material increases with increases in hardness, fatigue resistance and also a reduction of grain size [7]. Compared with their coarse-grained counterparts, nanocrystalline coatings exhibit a good combination of strength and toughness, as well as wear and corrosion resistance due to their more uniform chemical elemental distribution and finer grained structure [8,9]. Hence, nanocrystalline coatings are suggested to have significant potential applications for cavitation erosion resistance. Among the range of surface modification methods currently available, the double-cathode glow discharge deposition technique has been demonstrated to be a simple tunable, yet powerful, tool to enhance both the wear and electrochemical corrosion resistance of alloys such as Ti-6Al-4V through the fabrication of a series of nanocrystalline metal silicide and ceramic coatings [10,11]. Notably, the addition of Al has been demonstrated to be a fruitful path to improve the cavitation-erosion resistance of $TaSi_2$ and β-Ta_5Si_3 nanocrystalline coatings by improving both their mechanical properties and corrosion resistance [12,13].

As is well known, transition metal nitrides are the most widely used candidates for wear- and corrosion-resistant coatings on structural components operating in extreme environments [14]. As a hard ceramic coating, NbN, that exhibits a very attractive combination of physical and chemical properties, has received much attention for its potential applications, including protective hard coatings in machining [15], as a diffusion barrier, as a field emission cathode in microelectronic devices [16] and in supercapacitors for energy storage systems [17]. Up to now, there have been only a limited number of reports concerning the corrosion and wear properties of NbN coatings [18]. Moreover, its corrosion behavior under cavitation erosion conditions is still almost completely unexplored.

Although transition metal nitrides coatings are known to possess high chemical inertness, they may be dissolved and transformed into oxynitrides or oxides in passive films when redox reactions take place on their surface during electrochemical corrosion under suitable aqueous solution conditions [19]. For passive materials, the stability of their passive films in corrosive media is closely related to their semiconducting behavior. Furthermore, during cavitation erosion, these surface passive films may undergo electrochemical dissolution and mechanical removal in the presence of cavitation, but may be subsequently reformed on damaged areas due to repassivation. Unfortunately, little attention has been paid to the relationships linking the electronic properties and the repassivation capability of passive films and the cavitation erosion resistance of transition metal nitride coatings.

In the present work, the potential application of NbN as a protective coating against ultrasonic cavitation erosion under marine environments has been explored. To do so, a reactive-sputter-deposited NbN nanoceramic coating was synthesized on to a Ti–6Al–4V substrate using a double-cathode glow discharge plasma method. The ultrasonic cavitation erosion performance of the coating was investigated in a 3.5 wt% NaCl solution using a range of electrochemical analytical methods, assisted by mass loss studies and cross-sectional observations of the eroded surface. This work focuses primarily on the relationship between semiconductive properties of the passive film formed on the NbN coating and its cavitation. To better understand the semiconductive properties of the passive film, the energy of vacancy formation and the adsorption energy of chloride ions for the passive film grown on the coating were determined by first-principles density-functional theory.

2. Experimental materials and methods

2.1. Coatings preparation

Ti-6Al-4V substrate was abraded with different SiC abrasive papers and mechanically polished with 0.5 μm Cr_2O_3 powder, followed by ultrasonically cleaning in acetone. The NbN coating was deposited using a double-cathode glow discharge system employing an elemental niobium plate as the target material. The pressure of working gas was 40 Pa and the working gas was composed of high-purity argon and nitrogen, with an Ar:N_2 flux ratio of 20:1. Synthesis of the NbN coating was conducted at a target bias voltage of 900 V, a substrate bias voltage of 300 V with impulse current and a deposition temperature of 750 ℃. The parallel distance between the target and the substrate was held at 8.5 mm. The time of deposition was 2 h.

2.2. Microstructural characterization

The phase analysis of the as-received coatings was carried out using an X-ray diffractometer (XRD) with a D8 ADVANCE diffractometer and XRD data was collected employing Cu-Kα radiation. The X-ray source was operated at 30 mA and 40 kV. SEM observation of the surface and cross-sectional morphologies of the as-synthesized coatings were performed using a field-emission SEM (FE-SEM Hitachi, S-4800, Japan), which included an energy dispersive spectrometer (EDS) attachment (EDX-4, Philips). A JEOL JEM-2010 transmission electron microscope operating at an accelerating voltage of 200 kV was used to characterize cross-sectional TEM samples from the coating that were fabricated using a focused ion beam (FIB) microscope (FEI xP200, FEI Company, Hillsboro, OR). X-ray photoelectron spectroscopy (XPS) spectra were acquired using an ESCALAB 250 spectrometer analyzer (Thermo VG Co, USA) with an Al Kα X-ray source ($h\nu = 1486.68$ eV).

2.3. Mechanical properties measurements

Evaluation of the hardness and elastic modulus of the NbN coating was undertaken with a nanoindentation tester (Ultra-Micro Indentation System 2000) using a Berkovich diamond indenter. Fused silica was employed as a standard for indenter calibration. The indentation testing was performed in the load control mode by applying the indenter with a loading rate of 40mN/min into the sample surface and to a 20 mN maximum load. The recorded indentation data were analyzed through the Oliver–Pharr method [20]. A scratch tester (WS-2005), that included with an acoustic emission (AE) detector, was applied to determine the adhesion strength between the NbN coating and the substrate.

2.4. Cavitation erosion tests

Ultrasonic cavitation erosion experiments were carried out using a JY92-IIDN magnetostrictive-induced cavitation apparatus (NingBo Scientz Biotechnology Co., Ltd.) resonating at 20 kHz using an amplitude of 60 μm. A naturally aerated 3.5 wt% NaCl solution was selected to simulate marine environments and the temperature of the test medium was kept at 25 ± 1 °C controlled by flowing cooling water. The total testing duration was 15 h for each specimen, with periodic weight loss measurements performed every hour using an analytical balance.

2.5. Electrochemical analyses

All electrochemical testing was undertaken using a CHI660C workstation (Shanghai ChenHua Instruments Inc., China) using a conventional three-electrode system, which consisted of a working electrode with an area of exposure of ~ 1.0 cm^2, a platinum foil as counter electrode and a saturated calomel electrode (SCE) as reference electrode. The potentiodynamic polarization and the electrochemical impedance spectroscopy (EIS) measurements were performed after different cavitation times at an output power of 800 W. The potentiodynamic polarization plots were measured in a range of −600 mV_{SCE} to +1.5 V_{SCE} with a sweep rate of 10 mV/min. EIS analysis was performed using perturbation amplitude of 10 mV in the frequency range from 100 kHz to 10 mHz at each respective OCP. The recorded EIS data were investigated by an appropriate electrical equivalent circuit (EEC) using the ZSimpWin software. Before the Mott-Schottky measurements were performed, the specimens were potentiostatically polarized at the investigated passive potentials for 1 h to form a steady-state passive film. Furthermore, the capacitance measurements for the samples were conducted at a frequency of 1000 Hz by sweeping the applied potential in the negative direction from the potential of the formed passive film up to −1.0 V_{SCE} with potential steps of 25 mV. Potential of zero charge (PZC) measurements were performed using a 10 mV peak-to-peak sinusoidal perturbation at a fixed frequency of 18 Hz.

2.6. Theoretical calculations

First-principles calculations were used to investigate the energy of formation of an oxygen vacancy and the adsorption energy for Cl^- ions on surface oxide films present on both the coating and the Ti-6Al-4V substrate. Theoretical calculations were performed by means of first-principles methods within the framework of density functional theory (DFT) as implemented using the Cambridge Sequential Total Energy Package (CASTEP) software [21]. The interactions between the ionic cores and the electrons were described by the projector augmented wave (PAW) method [22], and a plane-wave cutoff energy was set to 340 eV. The reciprocal space sampling was done with a k-points mesh generated by the Monkhorst–Pack method [23]. To achieve good convergence, grids with dimensions of 5 × 5 × 8, 4 × 2 × 1, 5 × 5 × 4 and 4 × 4 × 1 were used for calculations of the bulk model for rutile TiO_2, a free rutile TiO_2 (1 1 0)-2 × 2 surface and a rutile TiO_2(1 1 0)-2 × 2 surface, including an O vacancy and Cl^- adsorption, the bulk model for the B-Nb_2O_5, a free B-Nb_2O_5 (0 1 0)-2 × 2 surface and a B-Nb_2O_5 (0 1 0)-2 × 2 surface including an O vacancy and Cl^- adsorption, respectively. The computational details are illustrated in Section 4 of the Supplementary materials.

3. Result and discussion

3.1. Microstructural characterization

Fig. 1(a) shows a typical XRD pattern taken from the binary NbN

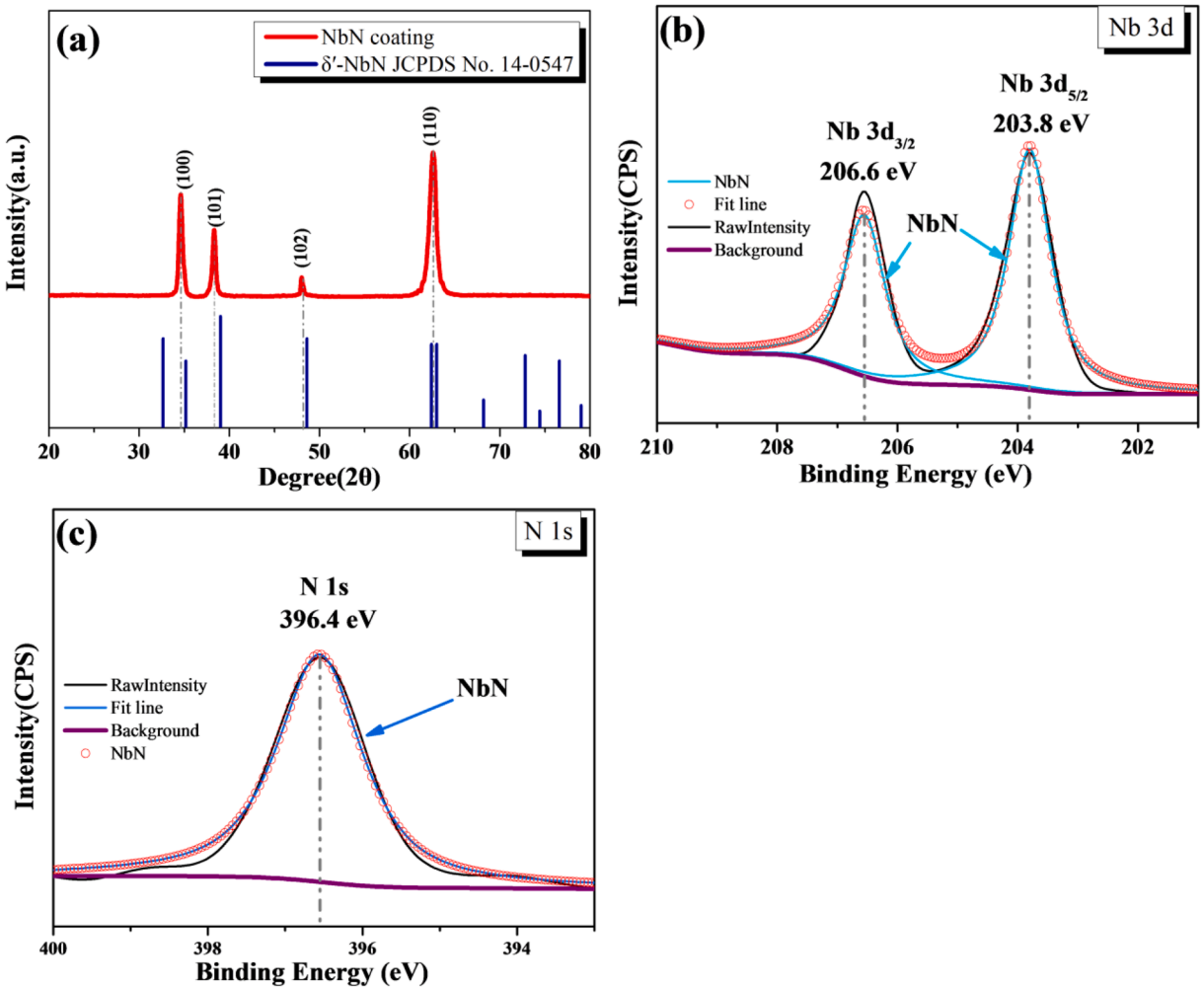

Fig. 1. (a) XRD pattern from the NbN coated specimen. High-resolution XPS spectra for the (b) Nb 3d and (c) N1s peaks collected from the NbN coating.

coating deposited on a Ti-6Al-4V substrate. For comparison, the standard XRD pattern for hexagonal wurtzite-type δ′-NbN (JCPDS Card No. 14–0547) is also displayed. Through referring to standard powder diffraction data, four distinct diffraction peaks can be indexed to the (1 0 0), (1 0 1), (1 0 2) and (1 1 0) reflections of a wurtzite-type hexagonal δ′-NbN phase. No peaks related to the presence of other niobium nitrides were detected in the XRD spectrum, suggesting phase purity of the NbN coating. Since the phase compositions in NbN system are very complex, the NbN films prepared by different deposition techniques often exhibit different crystalline structures, including cubic, tetragonal and hexagonal structures or the co-existence of cubic and hexagonal structures, depending on deposition parameters such as substrate bias [24], nitrogen partial pressure [25] and deposition temperature [26]. Previous studies have shown that a phase transition from face-centered cubic structured δ phase to a hexagonal structured δ′ phase for as-deposited NbN films occurs with increasing substrate bias, nitrogen partial pressure and deposition temperature. Those observations are consistent with our XRD data, because of the high deposition temperature, substrate bias and nitrogen partial pressure employed in this study. As compared to the standard peak positions, the positions of the diffraction peaks of δ′-NbN are shifted slightly towards lower 2θ angles. Such a slight deviation is assigned to the presence of compressive stresses intrinsically generated during deposition.

In addition, it can be seen from Fig. 1(a) that intense peaks resulting from the (1 0 0) and (1 1 0) lattice planes could be detected in the XRD spectrum, compared to the corresponding powder diffraction spectrum, suggesting the existence of a mixture of (1 0 0) and (1 1 0) crystallographic textures in the coating. In order to further quantify the degree of preferential growth of the coating, the texture coefficient (TC_{hkl}) of a given (*hkl*) reflection plane was determined using the Harris method [27], expressed by the following formula:

$$TC_{hkl} = \frac{I_m(hkl)/I_0(hkl)}{\frac{1}{n}\sum_1^n I_m(hkl)/I_0(hkl)} \quad (1)$$

where n is the total number of diffraction peaks considered in the analysis, I(hkl) and I_0(hkl) refer to the measured integrated intensity from the NbN coating and standard intensity obtained from the JCPDS data for a given (*hkl*) plane, respectively. Table 1 summarizes the calculated TC_{hkl} values for the NbN coating. As shown in Table 1, only the calculated TC values of (1 0 0) and (1 1 0) planes are greater than 1, signifying that the NbN coating shows strong (1 0 0) and (1 1 0) preferred orientations. From thermodynamic and kinetic standpoints, the texture developed in polycrystalline coatings is governed by the competition between surface and strain energies [28]. As noted above, owing to the presence of the compressive stress, the preferential growth of the NbN coating may be mainly regulated by strain energy, which is a major contributor to the total Gibbs free energy. Wen et al. [24] confirmed that under compressive stress conditions, the *c* axis of δ′-NbN lying in the plane of the coating (i.e. the angle between *c* axis and the normal to the stress plane is 90°) was the more energetically favorable configuration to achieve the lowest strain energy, leading to the formation of (1 0 0) and (1 1 0) preferred orientations. This is consistent with our experimental results.

To determine the chemical state and chemical composition of the coating, XPS analysis was conducted on the as-received NbN coating after sputtering with a 3 keV Ar^+ ion beam for 300 s. Fig. 1(b) and (c) present the high-resolution XPS spectra obtained from Nb 3d and N 1 s core levels, respectively. For the Nb 3d core level spectrum, a doublet with the Nb $3d_{5/2}$ and Nb $3d_{3/2}$ peaks located at 203.8 and 206.6 eV, respectively, with a Nb $3d_{5/2}$/ Nb $3d_{3/2}$ area ratio of 3:2, represents the Nb-N bonds in niobium nitride [29]. As can be seen from the N 1 s spectrum (Fig. 1 (c)), a single peak located at a binding energy of 396.4 eV is present that can be assigned to nitrogen atoms bonded to niobium [29]. Based on the relative atomic concentration measured from the Nb 3d and N1s XPS peak areas, the atomic ratio of N to Nb was measured to ~ 0.88.

Table 1
The calculated texture coefficients (TChkl) for different planes of the NbN coating.

	(1 0 0)	(1 0 1)	(1 0 2)	(1 1 0)
TC_{hkl}	1.55	0.63	0.23	1.60

Fig. 2 shows a typical cross-sectional SEM image, in backscattered electron mode, and a corresponding EDS elemental map of the as-prepared NbN coating deposited on a Ti-6Al-4V substrate. From this image, the coating appears to be very dense and homogeneous with no visible defects present at the coating/substrate interface. The EDS elemental maps suggest that Nb and N are distributed homogenously across the coating. Further, closer examination of EDS elemental maps for Nb and Ti indicate that there is a mutual diffusion of these elements across the interface between the coating and the substrate.

To investigate the microstructure of the NbN coating in more detail, analysis by cross-sectional TEM was performed, including investigation of the coating/substrate interface (Fig. 3). It can be seen that the interface between the NbN coating and titanium substrate is uniform, clean and free of any deleterious chemical reaction. The coating exhibited two distinct regions across the coating cross-section, namely, a (Ti,Nb)N diffusion interlayer and a δ′-NbN deposition layer. The interface between the coating and substrate presented as a 2 μm thick diffusion interlayer (Fig. 3(d)) that exhibited equiaxed grains with an average grain size of 107 nm. By combining these observations with analysis by selected area electron diffraction (insets in Fig. 3(i) and Fig. 3(j)) with the EDS measurements (line scan (Fig. 3(e)) and point (Fig. 3(g) and Fig. 3(h)) analyses), the darker and brighter contrast from the equiaxed grains are consistent with the presence of face-centered cubic (fcc) Ti-enriched (Ti,Nb)N and Nb-enriched (Ti,Nb)N phases with a B1-NaCl (rock salt) structure, respectively. The formation of the δ-(Ti, Nb)N layer is attributed to mutual interdiffusion of Ti and Nb and the high solid solubility of Ti in δ-NbN and Nb in δ-TiN. In the case of the δ′-NbN deposition layer (Fig. 3(b)), a pronounced columnar structure can be easily distinguished and the growth of those columns extends to the coating outer surface. A high-resolution transmission electron microscopy (HRTEM) image (Fig. 3(c)) demonstrates that those columns are formed by agglomerates of many elongated grains with their long axis aligned approximately parallel to the coating growth direction. Within a given column the elongated grains have similar orientations with an average diameter of about 10 nm. Analysis of the electron diffraction pattern (an inset in Fig. 3(b)), indicates that the interplanar spacings of the three strongest diffraction rings from closely match with the (1 0 0), (1 0 1) and (1 1 0) Bragg reflections for hexagonal δ′-NbN, respectively. Moreover, the incomplete arc-like rings corresponding to the (1 0 0) and (1 1 0) planes show greater diffracted intensity, confirming that the coating exhibits a mixed texture of (1 0 0) and (1 1 0), in agreement with the data obtained from XRD. The spacing of the lattice fringes shown in the bright-field HRTEM image was measured to be 0.256 nm, which is consistent with the theoretical *d* spacing for the (1 0 0) plane for hexagonal δ′-NbN. Also, the above analysis suggests that the phase transition from hexagonal δ′-NbN to cubic δ-NbN may occur at the diffusion layer, because of the substitution of Nb atoms by Ti atoms in the δ′-NbN lattice.

3.2. Mechanical properties

The nano-indentation tests indicate that the hardness (H) and elastic modulus (E) of the NbN coating were shown to be 36.8 ± 1.4 GPa and 407.6 ± 18.9 GPa, respectively, which is similar to values for a δ′-NbN coating prepared by reactive magnetron sputtering [15] (see Fig. S2(a) in the Supplemental material). Generally, the hexagonal structured δ′-NbN coating exhibits higher intrinsic hardness compared to the *fcc*-structured δ-NbN coating (25 GPa), which may be associated with its

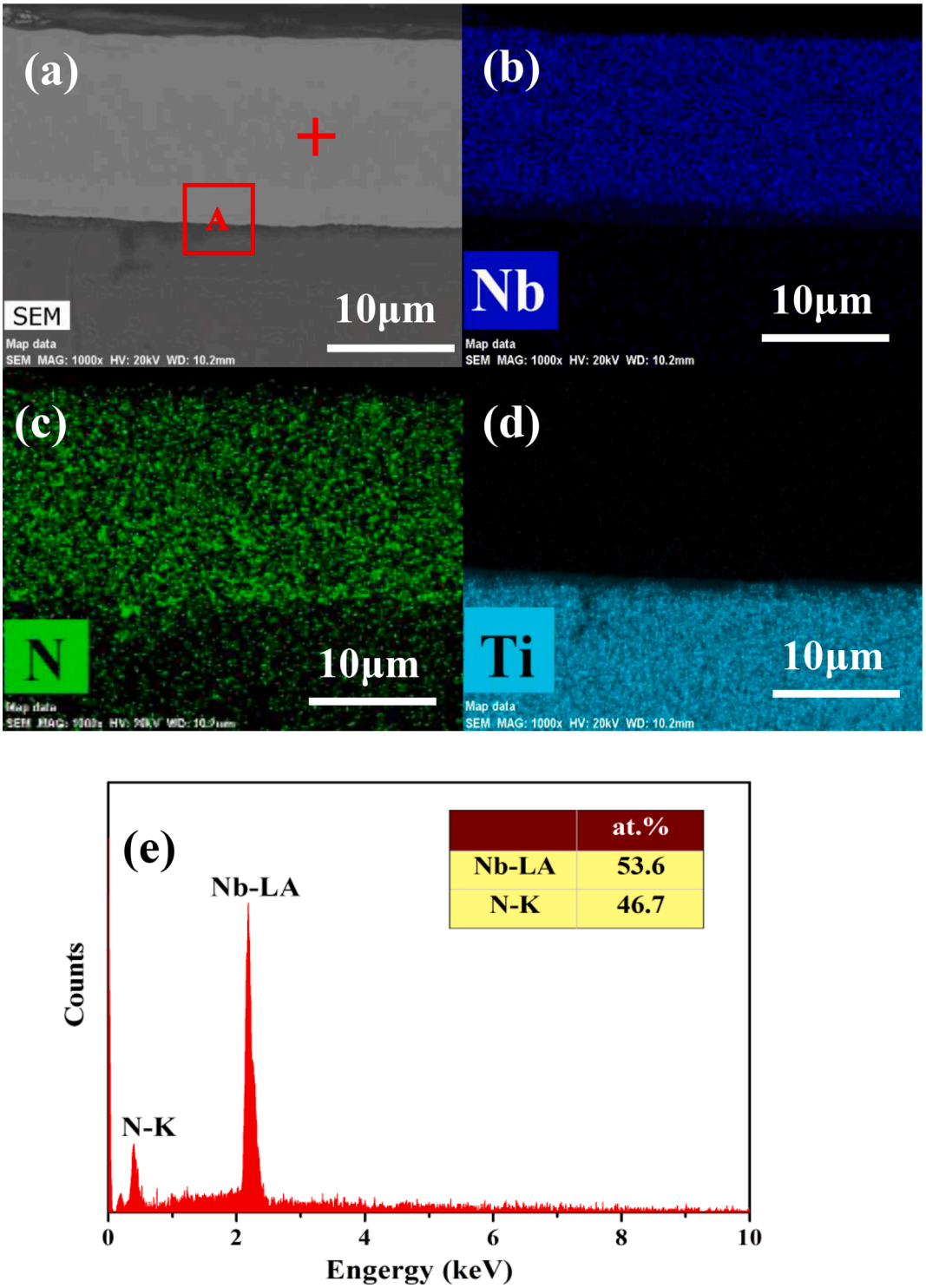

Fig. 2. (a) SEM cross-sectional image of the NbN coating and the corresponding EDS elemental maps for (b) Nb, (c) N and (d) Ti. (e) EDS point spectrum taken from region marked by "+" in Fig. 2a.

higher shear modulus and stronger covalent character for δ′-NbN [30].

During the cavitation erosion process, cavitation attack may be conceived as a series of high-velocity nano- or micro-indentations. For this reason, several studies have shown that the mechanical indexes, composed of a series of the ratios between hardness and elastic modulus, including H/E, H^2/E and H^3/E^2 ratios, play an critical role in predicting the cavitation erosion resistance of a hard coating [2]. The values of H/E, H^2/E and H^3/E^2 are greater for the NbN coating than for the values reported by others [15,24,29,31,32](see Fig. S2(b) in the Supplemental material). In light of these parameters, one might anticipate that a greater energy of the collapsing bubbles is required to cause deformation of the NbN coating prepared in this study as compared to other NbN-based coatings.

From the acoustic emission signal versus scratching load plot (see Fig. S3 in the Supplemental material), little noise is detected when the applied scratch load is less than 84 N, but above this value, strong acoustic signals emerge. The scratch pattern corresponds well with the acoustic emission signals, which suggests that the critical load for

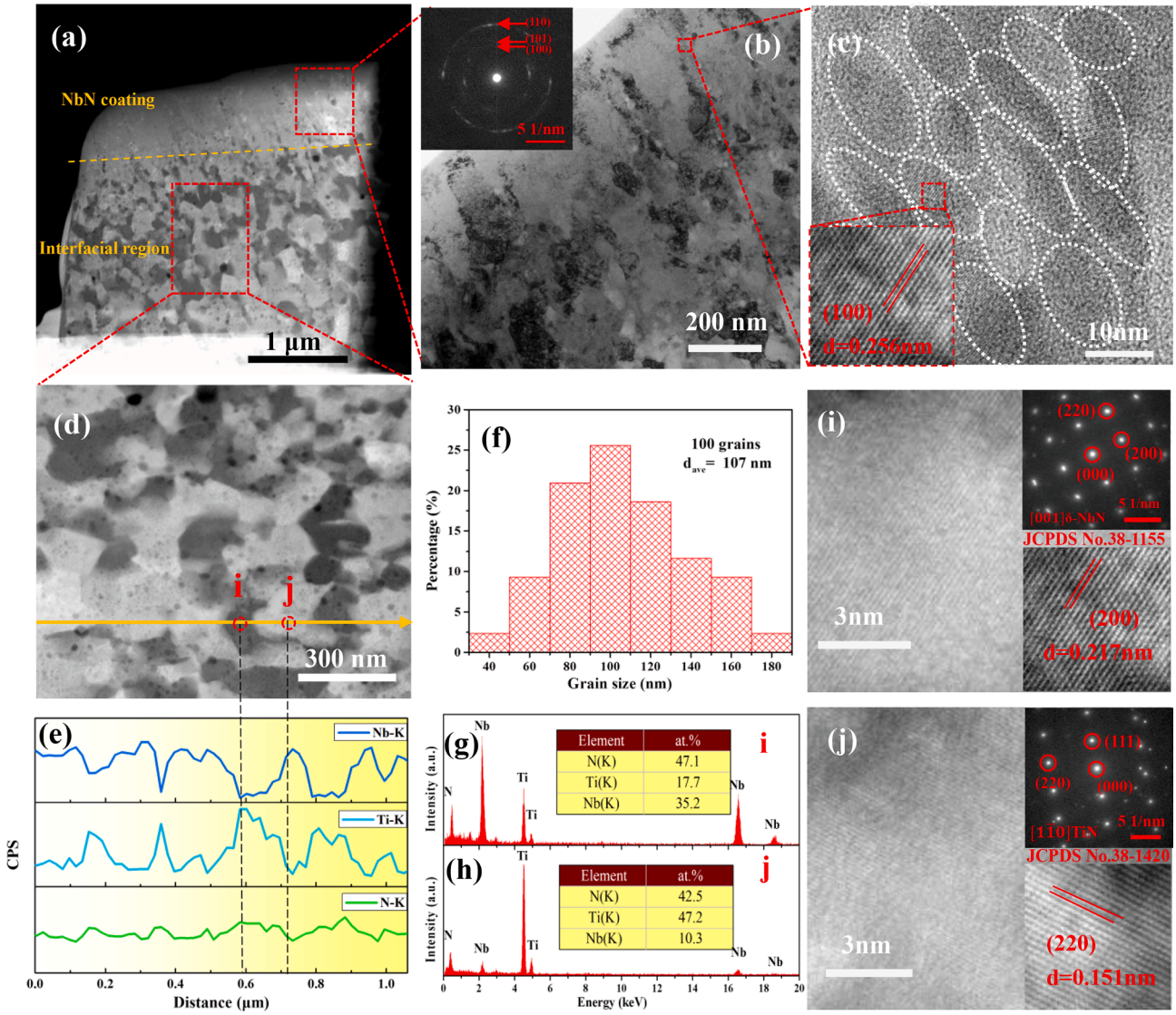

Fig. 3. (a) Dark field STEM image showing the NbN coating /substrate interfacial region (from the area marked "A" in Fig. 2a). (b) Bright field TEM image of the NbN coating from the region identified in (a) (insert shows SAED pattern). (c) High-resolution TEM image of the area identified in (b). (d) High resolution STEM image of the interfacial area identified in (a). (e) Elemental concentration profiles along the direction (shown in d) measured by an EDS line-scan. (f) Statistical histogram of the grain sizes in shown in (d). EDS spectra obtained from area (g) shown in (i) and area (h) shown in (j) of regions marked in (d). High-resolution TEM images and the SAED patterns (shown in the insert) of area (i) and area (j) identified in (d).

adhesive failure of the NbN coating is ~ 84 N. This critical load value is much greater than that usually suggested to be required for sliding contact applications (that is, a critical load of 30 N measured by a standard Rockwell-C indenter) [33].

3.3. Electrochemical corrosion behavior

3.3.1. Open circuit potential (OCP) measurements

To further clarify the effect of cavitation on the OCP value, the evolution of the OCP values with immersion time for the NbN coating and bare Ti-6Al-4V in a 3.5 wt% NaCl solution were monitored under conditions of cavitation cycle (alternating cavitation for 90 s and quiescence for 30 s), as presented in Fig. 4. As shown in Fig. 4(a) and (c), for each cavitation cycle, the corrosion potentials of the NbN coating go toward more noble values at the onset of the cavitation process and subsequently attain relatively stable values, but when the cavitation is stopped, the corrosion potential shifts quickly in the active direction. The change of OCP values caused by cavitation erosion depends on the balance of the anodic and cathodic currents. When the cavitation starts, the increased mass transfer of oxygen induced by the formation and subsequent collapse of cavitation bubbles accelerates the cathodic reduction reaction from dissolved oxygen. The electrons consumed by the cathodic reaction are supplied by the anodic oxidation, thereby the corrosion potentials of the tested samples move towards a positive direction. An enhancement of cathodic reaction can accelerate the rate of anodic oxidation reaction and oxide formation under cavitation conditions. Subsequently, oxide film formation is counterbalanced by its destruction induced by shockwaves and the microjets, and hence a relatively stable corrosion potential is achieved. When the cavitation is interrupted, the corrosion potentials shift quickly towards more negative values than typical OCP values corresponding to the non-cavitated coating. This may be interpreted as a significant decrease in the mass transport of oxygen and cathodic reaction rates. Therefore, under cavitation conditions, the main fluctuations of OCP values for the NbN coating are mainly regulated by the mass transport of oxygen. Such changes in potential are similar to that of some alloys or thermal spray coatings in a NaCl-based solution [34]. Nevertheless, in the case of bare Ti-6Al-4V (shown in Fig. 4(b) and (d)), the corrosion potentials move

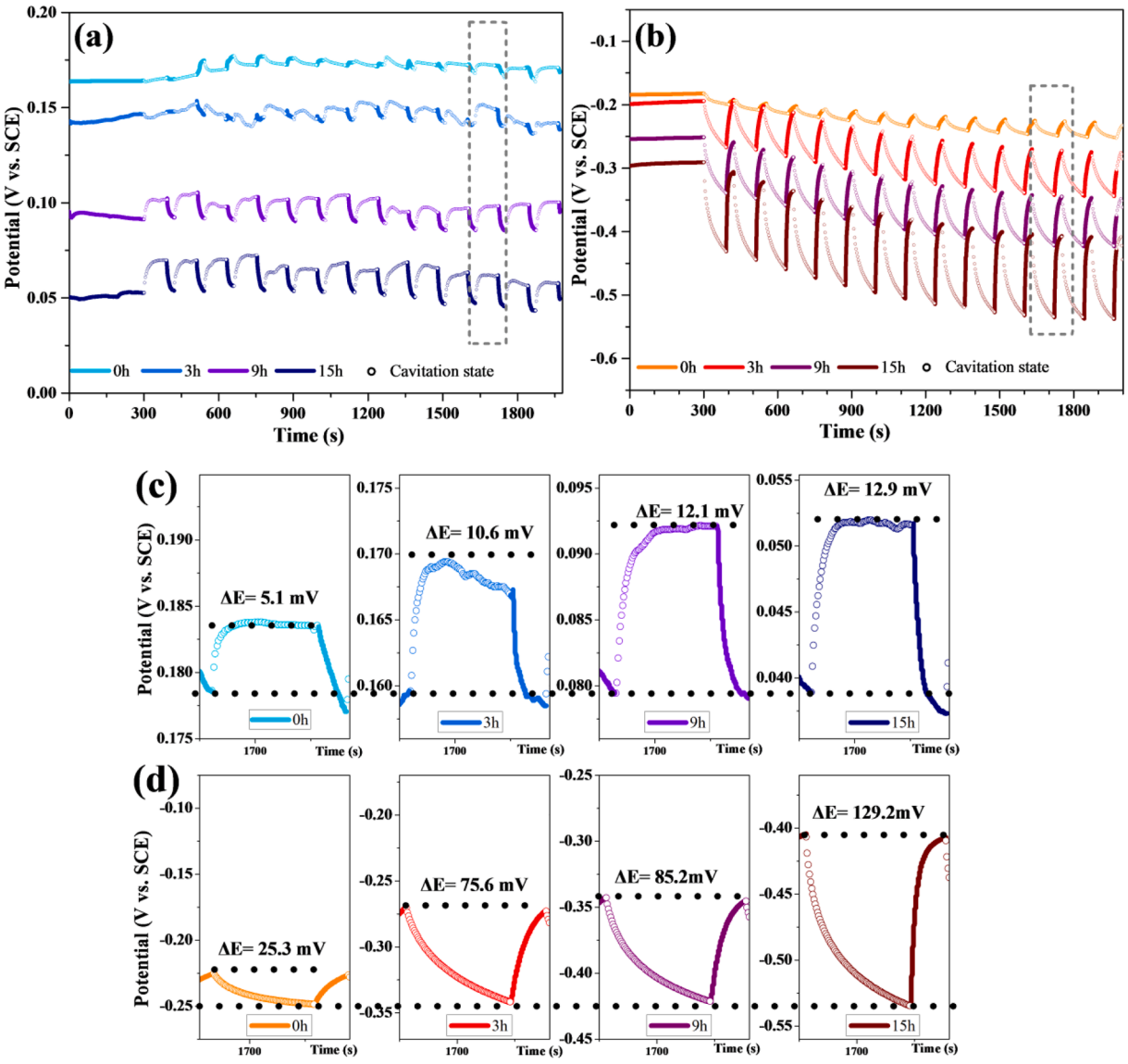

Fig. 4. The E_{OCP} vs. time plots for (a) the NbN coating and Ti-6Al-4V substrate (b) under the cavitation erosion cyclic conditions with the duty cycle of 75% (90 s ON and 30 s OFF) at an output power of 800 W in a 3.5 wt% NaCl solution. (c) The E_{OCP} vs. time plots for the NbN coating and the Ti-6Al-4V substrate for one cycle of cavitation erosion.

sharply towards the cathodic direction when cavitation is present and return immediately toward more positive values at the onset of the quiescence mode. Such shifts are mainly because the degradation of the uncoated Ti-6Al-4V surface is induced by the repetitive impacts of the microjets or shockwaves and this stimulates an active dissolution reaction ($M \rightarrow M^{n+}+ne$)t he electrochemical corrosion) In this situation, the electrochemical corrosion process of bare Ti-6Al-4V is largely controlled by the anodic reaction, because the passive film destruction has more influence than that of the mass transfer of oxygen under cavitation. A similar phenomenon has previously been observed on a 17–4 PH stainless steel substrate in a 3.5 wt% NaCl solution [35].

3.3.2. *Electrochemical polarization measurements*

To better understand the effect of cavitation erosion on the reaction kinetics, potentiodynamic polarization measurements were performed on the NbN coating and bare Ti-6Al-4V in a 3.5 wt% NaCl solution after different cavitation exposure times under quiescence conditions, as show in Fig. 5. The corresponding electrochemical kinetic parameters were obtained from the potentiodynamic polarization curves, such as corrosion potential (E_{corr}), corrosion current density (i_{corr}), anodic (β_a) and cathodic (β_c) Tafel slopes and polarization resistance (R_p), and are summarized in Table 2. It is evident that after different cavitation exposure times, the anodic polarization curves of both the coating and bare Ti-6Al-4V are characteristic of passive materials, without an active–passive transition, suggesting that both samples exhibit a clear self-passivating behavior in a 3.5 wt% NaCl solution. The cathodic polarization curves for the two samples are similar in shape and are superimposed on each other. Because the tested electrolyte is an aerated neutral solution with a low concentration of H^+ ions, the dominant cathodic reaction can be identified as the reduction of dissolved oxygen and water. Further, the theoretical value of cathodic Tafel slopes ($-\beta_c$), corresponding to the hydrogen evolution reaction, is 120 mV/decade, which is apparently lower than that for the tested specimens (listed in Table 2). By prolonging the cavitation period, the anodic branches shift towards the region of more negative potential and higher anodic current density, suggesting that detachment or dissolution process of passive films formed on the tested samples is increasing. As shown in Table 2, the change in β_a values with increasing cavitation time is more obvious than that for $-\beta_c$ values, implying that an extension of cavitation erosion has a more pronounced effect on the anodic reaction process than the

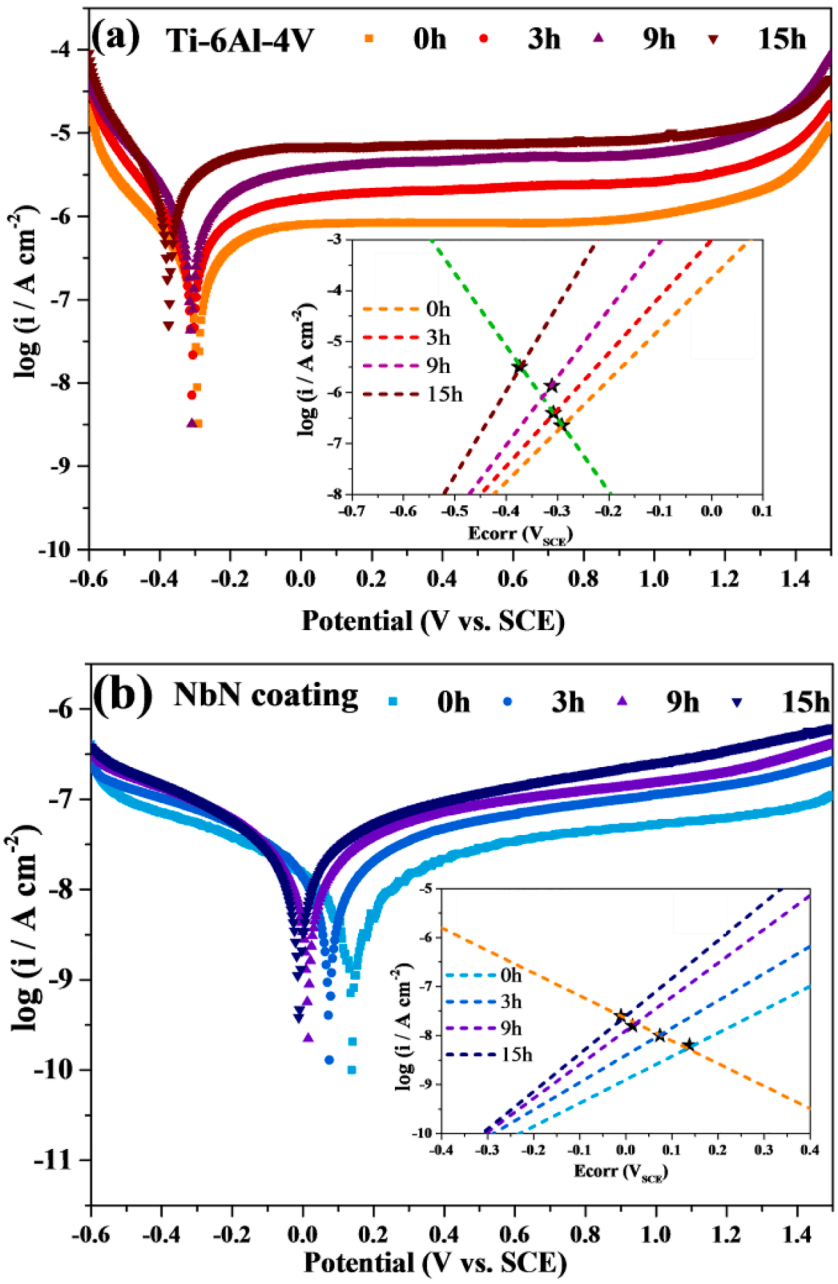

Fig. 5. The potentiodynamic polarization curves and the ideal schematic mechanism of the anodic and cathodic polarization curves for (a) uncoated Ti-6A1-4V and (b) the NbN coating before and after cavitation erosion of 3 h, 9 h and 15 h, respectively, with an output power of 800 W in a 3.5 wt% NaCl solution.

Table 2
Electrochemical parameters for the NbN coating and uncoated Ti-6Al-4V obtained from the potentiodynamic polarization curves.

	Cavitation time	E_{corr} (V_{SCE})	i_{corr} (A cm-2)	β_a (mV/decade)	-β_c (mV/decade)	R_P ($\Omega \cdot cm^2$)
NbN coating	0 h	0.138	6.319×10^{-9}	196.4	217.2	7.09×10^6
	3 h	0.074	9.977×10^{-9}	192.3	216.8	4.44×10^6
	9 h	0.014	1.585×10^{-8}	190.5	217.5	2.78×10^6
	15 h	−0.011	2.512×10^{-8}	190.0	216.6	1.75×10^6
Ti-6Al-4 V	0 h	−0.292	2.144×10^{-7}	163.5	220.1	1.90×10^5
	3 h	−0.308	3.808×10^{-7}	152.9	226.8	1.04×10^5
	9 h	−0.311	1.346×10^{-6}	149.7	224.7	2.89×10^4
	15 h	−0.374	3.078×10^{-6}	145.8	221.5	1.24×10^4

cathodic reaction process. According to the mixed potential theory, such a variation of Tafel slopes with cavitation time makes E_{corr} shift potential towards the cathodic direction. This is consistent with the data obtained from the OCP versus cavitation time curves (as shown in the inset in Fig. 5). For a given cavitation time, the E_{corr} value for the NbN coating is nobler than that for bare Ti-6Al-4V, and its i_{corr} value decreases by two orders of magnitude as compared to that for uncoated Ti–6Al–4V. This result indicates that the NbN coating is kinetically less active than bare

Ti–6Al–4V in a 3.5 wt% NaCl solution. Additionally, the corrosion resistance can also be evaluated from the R_p value, which is inversely proportional to corrosion rate. From Table 2, the R_p value of the coating is one to two orders of magnitude larger than that for bare Ti–6Al–4V, indicating that the NbN coating possesses higher chemical inertness and thus acting to provide effective protection against corrosion damage under cavitation erosion conditions.

3.3.3. XPS analysis of passive films

In order to gain detailed insight into the changes in the principal constituents of the passive films with applied potentials and cavitation times, XPS analysis was performed on the NbN coating both after potentiostatic polarization at different potentials for 120 min and after different cavitation erosion times in a 3.5 wt% NaCl solution, as shown in Fig. 6. As shown in Fig. 6(a), the XPS survey spectra reveal the presence of Nb 4p, Nb 3d, Nb 3p, N1s, O1s and C1s peaks. The C1s peak at 284.6 eV, corresponding to the presence of C–C bonds, stems from carbon contamination covering the surface of the tested coatings. After deconvolution of the Nb 3d core level spectra (Fig. 6(b)), it can be seen that Nb 3d peaks recorded from the passive films formed at applied potentials of +0.4 V_{SCE} and +0.6 V_{SCE} that can be systematically decomposed into three sets of doublets for Nb $3d_{5/2}$ and Nb $3d_{3/2}$, amongst which the Nb $3d_{5/2}$ peaks located at 203.8 eV, 206.5 eV and 207.5 eV can be assigned to NbN, NbO_xN_y and Nb_2O_5 [36]. For the passive films grown at an applied potential of +0.8 V_{SCE}, only one doublet corresponding to Nb_2O_5 is observed in the Nb 3d core level spectrum. Note that the detected NbN signal may arise from the coating beneath the passive films. With the increase of applied potential, the detected signals for NbN and NbO_xN_y decrease and signals for Nb_2O_5 increase accordingly, suggesting that the thickness of the passive films increases and the anodic oxidation reaction may proceed more thoroughly with increasing applied potential. As can be seen from Fig. 6(c), the high-resolution spectrum for N1s obtained from the passive films formed at applied potentials of +0.4 V_{SCE} and +0.6 V_{SCE} can be divided into three components with the corresponding binding energies of 396.5 eV, 397.5 eV, 400 eV, which can be assigned to N-Nb bonds in NbN, N-O bonds in NbO_xN_y and N–H bonds in NH_3 ligands (perhaps indicating the presence of NH_4^+ via further protonation) [37]. For the passive films formed at applied potentials of +0.8 V_{SCE}, only a single N1s peak at a binding energy of 400 eV was detected, which is consistent with the N chemical state in NH_3. The O 1 s spectrum (Fig. 6(d)) recorded on the passive films formed at applied potentials of +0.4 V_{SCE} and +0.6 V_{SCE} can be fitted to three distinct contributions at 530 eV, 531.3 eV and 533 eV, originating from the O-Nb bonds in Nb_2O_5, N-O bonds in NbO_xN_y and adsorbed water, respectively [37]. For the passive film formed at applied potentials of +0.8 V_{SCE}, the O 1 s core level region consists of two peaks at binding energies of 530 eV and 533 eV, indicating that the passive film consists principally of Nb_2O_5 at higher applied potentials. Fig. 6(e) and (f) show the XPS survey spectrum and Nb 3d XPS spectrum collected from the surface of the NbN coating after different cavitation erosion times in a 3.5 wt% NaCl solution, respectively. Similar to the results shown in Fig. 6(a), the signals for Nb 4p, Nb 3d, Nb 3p, N1s, O1s and C1s peaks appear on the surface of the NbN coating after 3 h, 9 h and 15 h of cavitation erosion in the 3.5 wt% NaCl solution. As shown in Fig. 6(f), in addition to small amounts of NbO_xN_y detected on the coating surface after 3 h of cavitation erosion testing, the passive films formed on the coating mostly consist of Nb_2O_5. This result indicates that under conditions of both potentiostatic polarization and cavitation erosion, a mixture of NbO_xN_y and Nb_2O_5 or a single Nb_2O_5 is the major constituent of the passive films. Based upon the principal constituent of the passive films grown on the NbN coating, the NbN coating may be oxidized during the potentiostatic polarization and cavitation erosion in a 3.5 wt% NaCl solution according to the following two possible hydrolysis reactions:

$$NbN + H_2O \rightarrow NbO_xN_y + NH_4^+ + OH^- \quad (2)$$

$$NbO_xN_y + H_2O \rightarrow Nb_2O_5 + NH_4^+ + OH^- \quad (3)$$

According to reaction (2), the partial oxidation of the NbN coating yields the intermediate product of NbO_xN_y at relatively low applied potentials or short cavitation erosion times and subsequently NbO_xN_y is further oxidized to Nb_2O_5 at higher applied potentials or during prolonged cavitation erosion.

3.3.4. Impedance analysis

To investigate the key role of the formed passive films on the cavitation erosion resistance of the NbN coating in 3.5 wt% NaCl solution, the electrochemical impedance spectra data, shown in Fig. 7, displayed through Nyquist, Bode-phase angle and Bode-impedance modulus diagrams, were determined at various cavitation times to monitor the passivation behavior of the coating surface. Nyquist plots of the NbN coated and the uncoated Ti-6Al-4V without cavitation testing show unfinished large capacitive loops and the corresponding Bode-phase versus frequency curves appear as a broad phase-plateau with maximum phase angle approaching −80° over a wide range of frequencies. This is indicative of typical capacitive behavior associated with the protective oxide film covering the tested sample, which is responsible for their large reaction resistance and low electrochemical corrosion rate under quiescent electrolyte conditions. In this case, the impedance spectra can be analyzed by an equivalent electric circuit (EEC) with a single time constant $R_s(R_fQ_f)$ as shown in Fig. 7(e), in which R_s is the solution impedance and R_f and Q_f are the polarization resistance and capacitance of the passive films formed on the tested samples, respectively. Because the presence of heterogeneities in the passive film promotes capacitance dispersion, a constant phase element (CPE) was used to obtain the best fit. From Table 3, after coating with NbN, the impedance value of Ti-6Al-4V increased by almost one order of magnitude, denoting that the passive film formed on the NbN coating exhibits more capacitive, insulating, resistant behavior than that for the bare substrate in a 3.5 wt% NaCl solution. When the tested samples are subjected to cavitation erosion, the Nyquist plots show more depressed capacitive arcs in the investigated frequency range, and the capacitive semicircles scale down with increasing cavitation erosion time. Simultaneously, with increasing cavitation erosion time, the phase plateaus in the mid-frequency range shown in Bode phase angle versus frequency plots become narrower with a reduction in the phase angle maximum and impedance modulus |Z| in the very low frequency range in Bode-impedance modulus plots decrease gradually. This suggests that the degradation in protective capability of the passive films grown on the samples tested is intensified at prolonged exposure times. At a given cavitation erosion period, the phase angle value for the NbN coating is appreciably larger than that for bare Ti-6Al-4V, implying a better resistive response derived from the more resistant passive film on the coating. Except for impedance data for the NbN coating after 15 h of cavitation testing, Bode phase angle plots registered for the cavitated samples consist of two-time constants. For bare Ti-6Al-4V, the Bode phase angle diagrams display two phase angle maxima in the low and middle frequency ranges with the higher maximal value of phase angles in the middle frequency range. Hence, a two R-Q element EEC ($Rs(Q_pR_p)(Q_bR_b)$) shown in Fig. 7(f) was used to model the electrochemical process for bare Ti-6Al-4V during the cavitation test. This EEC assumes the formation of the duplex oxide film on bare Ti-6Al-4V due to the cavitation destruction, which is composed of an inner, compact, insulating layer together with an outer, porous, less protective layer. This EEC describes two electrochemical reactions with different time constants, among which one reaction (Q_pR_p) occurs at the porous outer layer/solution interface in the middle frequency range and the other one (Q_bR_b) occurs at the interface between the dense inner layer and the Ti-6Al-4V substrate. For the NbN coating after 3 h and 9 h of cavitation exposure, the Bode phase angle plots are composed of two overlapping peaks with the higher maximal value of phase angles appearing in the low frequency range. Nonetheless, only one symmetric peak was observed over

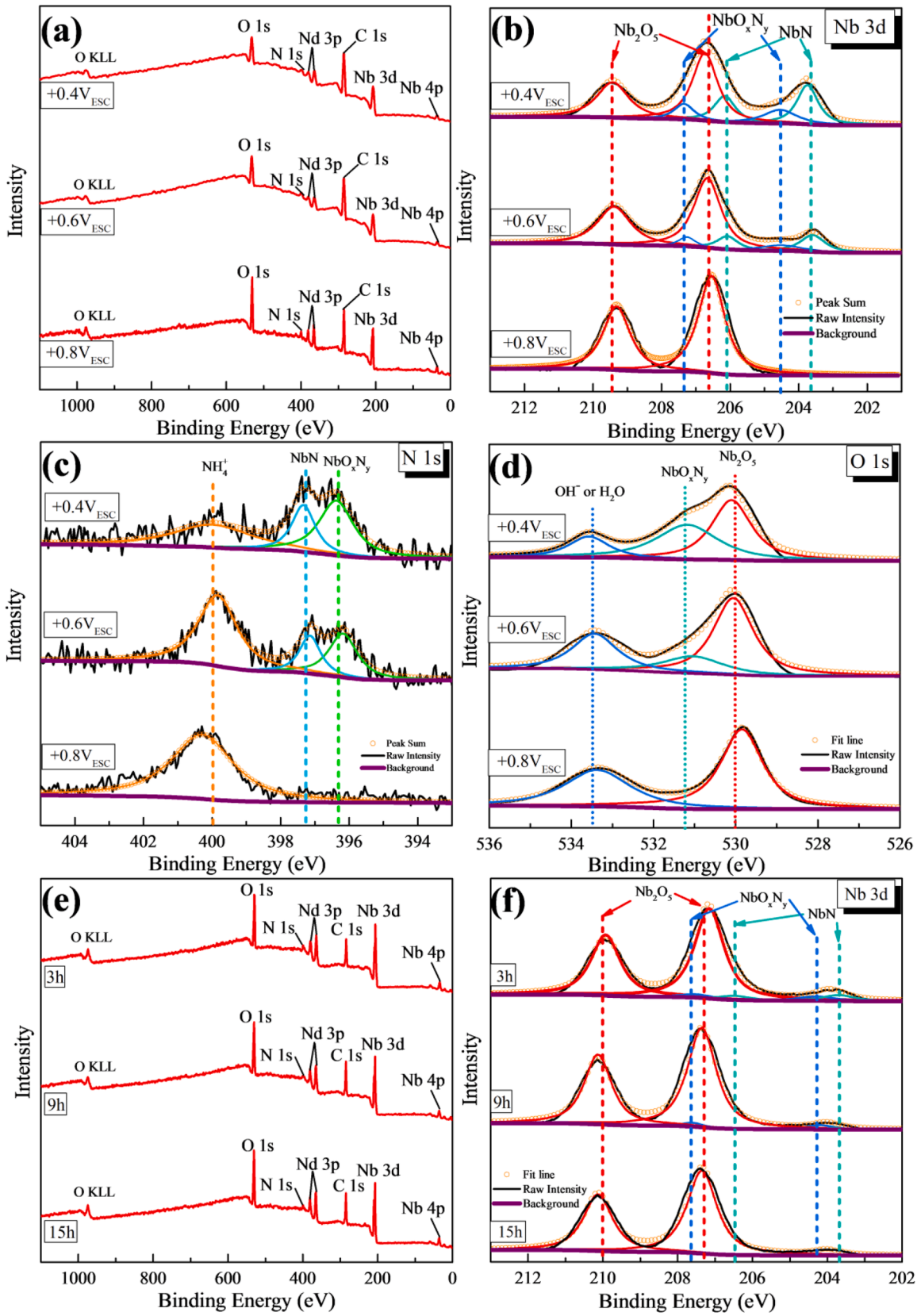

Fig. 6. (a) XPS survey spectra and high-resolution XPS spectra for (b) Nb 3d, (c) N 1 s and (d) O 1 s peaks for the NbN coating after potentiostatic polarization with 120 min at 0.4 V_{SCE}, 0.6 V_{SCE} and 0.8 V_{SCE}, respectively, in a 3.5 wt% NaCl solution. (e) XPS survey spectra and the (f) high-resolution XPS spectra for Nb 3d peaks collected from the NbN coatings after cavitation erosion for 3 h, 9 h and 15 h, respectively, with an output power of 800 W in a 3.5 wt% NaCl solution.

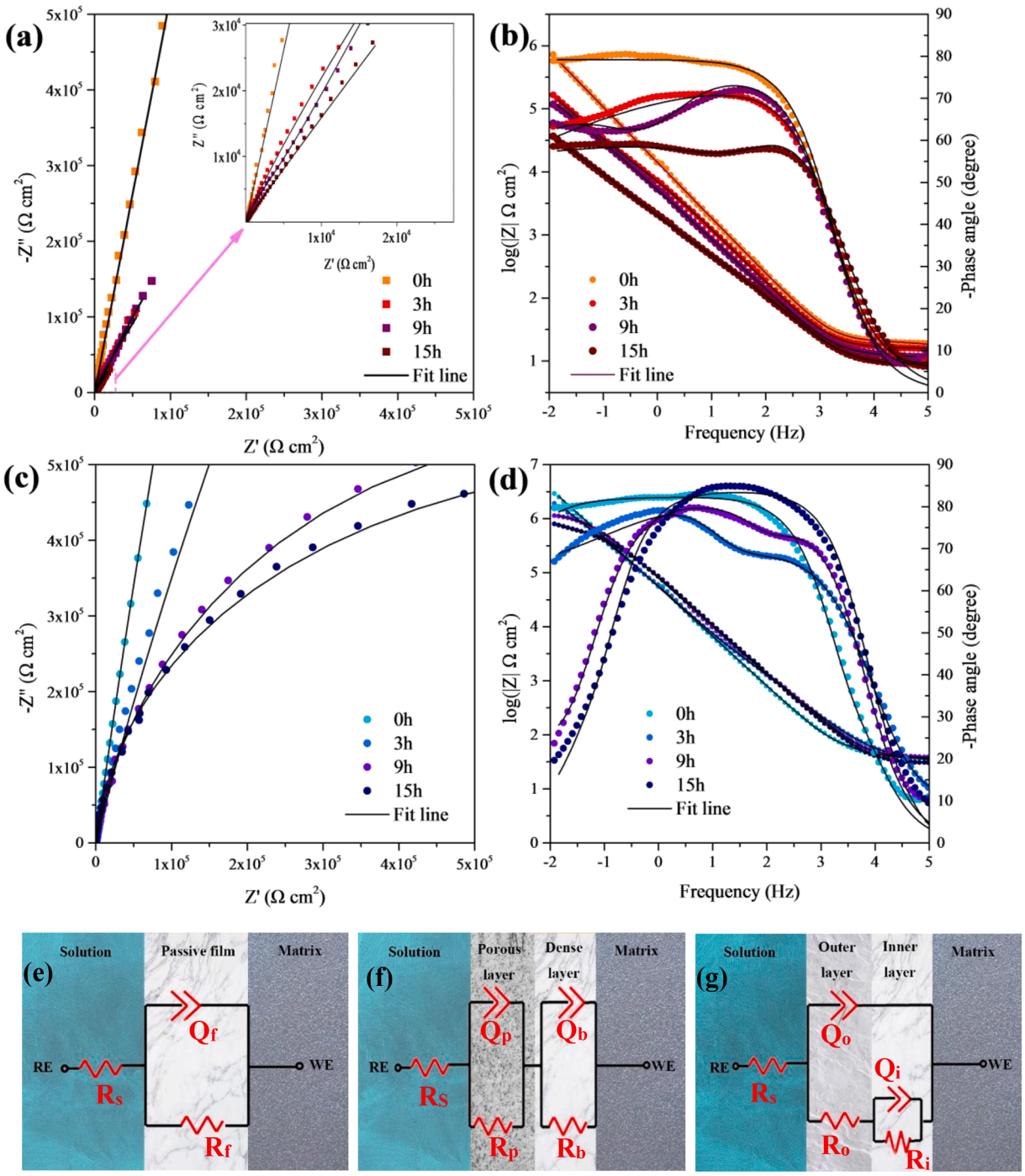

Fig. 7. (a and c) Nyquist and (b and d) Bode plots collected from uncoated Ti-6Al-4V and the NbN coating in a 3.5 wt% NaCl solution before and after different times of cavitation erosion with an output power of 800 W. (a and b) the NbN coating, (c and d) uncoated Ti-6Al-4V. The equivalent electrical circuits (e) $R_s(Q_iR_f)$, (f) $R_s(Q_pR_p)(Q_bR_b)$ and (g) $R_s(Q_o(R_o(Q_iR_i)))$ used for modeling experimental EIS data.

the investigated frequency ranges for the coating after 15 h of cavitation exposure. According to the results of XPS analysis, one might speculate that after 3 h and 9 h of cavitation exposure, the passive oxide films consist of an outer Nb_2O_5 layer and an inner NbO_xN_y layer, whereas the passive film is composed of a single Nb_2O_5 layer after 15 h of cavitation exposure. Therefore, the impedance spectra recorded after 3 h and 9 h of cavitation exposure were modelled with an EEC ($R_s(Q_o(R_o(Q_iR_i)))$), shown in Fig. 7(g), and an EEC model shown in Fig. 7(e) was used for describing the EIS spectra obtained following 15 h of cavitation exposure. From the fitted equivalent circuit parameters illustrated in Table 3, the overall resistance values (i.e., R_f, $R_p + R_b$ and $R_o + R_i$), reflecting the resistive contributions of the passive films, for both the NbN coated and uncoated substrate decrease with increases in cavitation exposure time, suggesting the decreased resistance of cavitation erosion with extending cavitation erosion period. Further, the CPE exponent, n, values, representing the level of defects in the passive film, also decrease with increasing time of cavitation erosion, indicating a gradual increase in the density of defects in the formed passive films. Rougher surfaces induced by the cavitation damage increase the cavitation exposure area, thereby speeding up the electrochemical corrosion reactions and decreasing charge transfer resistance. For a given cavitation erosion time, the resistance and n values for the NbN coating are significantly

Table 3
Electrochemical parameters obtained from numerical fitting for NbN coatings and uncoated Ti-6Al-4 V after different times of cavitation erosion at an input power of 800 W in a 3.5 wt% NaCl solution.

Ti-6Al-4 V		$R_s(Q_fR_f)$						
		Rs (Ω cm^2)	Q_f (Ω^{-1} cm^{-2} s^n)	R_f (Ω cm^2)	n			
	0 h	38.22	1.43×10^{-5}	6.71×10^{5}	0.88			
		$R_s(Q_pR_p)(Q_bR_b)$						
		Rs (Ω cm^2)	Q_p (Ω^{-1} cm^{-2} s^n)	R_p (Ω cm^2)	n_1	Q_b (Ω^{-1} cm^{-2} s^n)	R_b (Ω cm^2)	n_2
	3 h	33.57	4.17×10^{-5}	192.13	0.78	3.71×10^{-5}	1.38×10^{5}	0.85
	9 h	34.91	6.82×10^{-5}	180.09	0.72	5.56×10^{-5}	7.36×10^{4}	0.83
	15 h	31.72	1.84×10^{-4}	168.48	0.69	1.49×10^{-4}	2.33×10^{4}	0.79
NbN coating		$R_s(Q_fR_f)$						
		Rs (Ω cm^2)	Q_f (Ω^{-1} cm^{-2} s^n)	R_f (Ω cm^2)	n			
	0 h	30.69	1.35×10^{-6}	4.77×10^{7}	0.97			
		$R_s(Q_o(R_o(Q_iR_i)))$						
		Rs (Ω cm^2)	Q_o (Ω^{-1} cm^{-2} s^n)	R_o (Ω cm^2)	n_1	Q_i (Ω^{-1} cm^{-2} s^n)	R_i (Ω cm^2)	n_2
	3 h	31.59	4.16×10^{-6}	7.74×10^{6}	0.91	3.07×10^{-6}	1.41×10^{7}	0.96
	9 h	37.62	2.56×10^{-5}	2.63×10^{6}	0.90	9.54×10^{-6}	8.66×10^{7}	0.94
		$R_s(Q_fR_f)$						
		Rs (Ω cm^2)	Q_f (Ω^{-1} cm^{-2} s^n)	R_f (Ω cm^2)	n			
	15 h	36.65	7.25×10^{-5}	1.17×10^{6}	0.87			

higher than those for the uncoated sample, denoting a higher corrosion protection capability of the passive film present on the coating.

3.4. Cumulative weight loss measurements and observations of eroded morphologies

The accumulative weight loss, plotted as a function of exposure time, for the NbN coating and uncoated Ti-6Al-4V after 15 h of cavitation exposure period in a 3.5 wt% NaCl solution under a given output power of 800 W is shown in Fig. S4 in the Supplemental material. Typically, the cavitation erosion process of a material can be divided into two periods, namely, incubation and propagation. The incubation period, defined as the shortest time period required for reaching a standard weight loss (1 mg/cm^2), is a key indicator in evaluating the cavitation erosion resistance of a material [38]. As shown in Fig. S4, the weight loss versus exposure time plot for uncoated Ti-6Al-4V shows an initial incubation period of about 4 h followed by a propagation period manifested by a rapid increase in weight loss with exposure time at a nearly constant rate. On the contrary, the weight loss for the NbN coating exhibits an extremely low rate of increase, almost independent of exposure time, and has not exceeded 0.3 mg/cm^2 in the tested duration. After 15 h of cavitation exposure, the overall weight loss for the NbN coating was nearly 30 times lower than that for the uncoated substrate. Therefore, the NbN coating provides Ti-6Al-4V with durable resistance to the initiation and propagation processes of cavitation damage.

To obtain a deeper insight into the possible cavitation degradation mechanism, SEM analysis was performed on the outer surface and specimen cross-section for the NbN coating and uncoated Ti-6Al-4V after different cavitation exposure times in a 3.5 wt% NaCl solution, which are shown in Fig. S5 and Fig. S6 in the Supplemental material, respectively. From Fig. S5(a ~ b) and Fig. S6(a ~ b), after cavitation exposure for 1 h, the original polishing traces remain visible on the eroded surface of uncoated Ti-6Al-4V, signifying little cavitation damage occurred on the duplex phases ($\alpha + \beta$) structure of Ti-6Al-4V. As the cavitation erosion time increased to 3 h, the eroded surface exhibited slight plastic deformation evident as surface undulations, with a number of small shallow micro-voids. The corresponding cross-sections for bare Ti-6Al-4V for 1 h and 3 h of cavitation erosion show a flat and smooth appearance, confirming further that the cavitation shock generated by the collapse of bubbles may mainly trigger increased internal stresses in the Ti-6Al-4V surface during the incubation period, in accordance with low material erosion rates following exposure to cavitation for 1 h and 3 h. The results also provide strong evidence of the duplex oxide film observed through EIS data, because the local corrosion process in micro-voids is responsible for the phase angle maxima in the middle frequency range. In the propagation period (shown in Fig. S5(c) and (d)), uncoated Ti-6Al-4V shows a rougher surface appearance with obvious signs of significant plastic deformation and large quantities of small cavitation pits and micro-cracks widely distributed on the eroded surface. For an $\alpha + \beta$ type Ti-6Al-4V alloy, β-Ti exhibits lower hardness than α-Ti, and the two phases have different responses to cavitation attack [5]. Under cavitation mechanical stresses, the β-Ti phase is preferentially removed and the remnant α phase is more vulnerable to cavitation attack, thereby facilitating the plastic deformation and with cavities evident in the eroded surface. As shown in Fig. S6(c) and (d), as the exposure time increases from 9 h to 15 h, fluctuant morphologies in cross-sections become more pronounced and more cavities are present on extruded regions. Such a rough surface not only leads to a greater surface area exposed to the corrosion medium, but also inhibits the formation of a dense passive film. Under the synergistic interaction of repeated mechanical impact and electrochemical corrosion, these extruded regions progressively lose the surrounding β-Ti phase and may be readily detached from the eroded surface, leading to higher material erosion rates in the propagation period. However, in contrast, after different cavitation erosion times, both the surface and cross-sectional structures of the NbN coating, as seen in Fig. S5(e ~ h) and Fig.S6(e ~ h), retain a smooth and compact structure, with no evidence of mechanical destruction or corrosion damage. This is consistent with its high resistance to plastic deformation shown in Fig. S2 in the Supplemental material. Moreover, once the passive film present on the coating is fractured by mechanical attack, the smoother eroded surface promotes faster re-passivation of the protective passive film and such a self-healing capability reduces the erosion rate of the coating in a 3.5 wt% NaCl solution.

3.5. Mott-Schottky analysis

To further investigate the reasons why the NbN coating exhibits better corrosion resistance compared to the uncoated Ti-6Al-4V substrate under cavitation erosion, some key parameters related to electronic properties of the passive films, including the concentration and the diffusivity of the defects, were investigated by Mott-Schottky analyses combined with a point defect model. According to the Mott-Schottky theory, if the capacitance of the space-charge layer is far lower than that of the double layer, the relationship between the space charge capacitance (C_{sc}) of a semiconductor and the applied electrode potential (E) under depletion conditions can be expressed as [39]:

$$C_{sc}^{-2} = \frac{2}{\varepsilon_r \varepsilon_0 e N}\left(E - E_{fb} - \frac{kT}{e}\right) \quad (4)$$

where C_{SC} is the space charge capacitance of the passive film, E is the applied electrode potential, e is the electron charge (1.6×10^{-19}C), N is the donor or acceptor density over a per unit volume (cm^{-3}), ε_r is the

dielectric constant of the passive film, ε_0 is the vacuum permittivity (8.854×10^{-14}F/cm). k is the Boltzmann constant (1.38×10^{-23} J/K), T is absolute temperature. kT/e is about 25 mV at room temperature and E_{fb} is the flatband potential of the passive film.

Fig. 8 shows the typical C_{SC}^{-2} versus E plots for the NbN coating and bare Ti-6Al-4 V after different cavitation exposure times and then subsequently polarized at different anodic potentials for 1 h in a 3.5 wt% NaCl solution. All these plots exhibit a positive slope over the entire potential range, suggesting that the passive films grown on the tested samples after different cavitation exposure times are typical of n-type semiconductor behavior. The n-type semiconductivity of these passive films suggests that oxygen vacancies are the dominant electronic charge carriers migrating through these passive films. In addition, there is a turning-point around $-0.4V_{SC}$ separating these Mott-Schottky plots into two linear regions with different slopes where the non-linearity arises from the ionization of surface states, the existence of deep doping levels and non-homogeneous doping [40,41]. In the linear region, above the inflection, the slopes of the linear regions are almost independent of the film formation potential, implying that the variation of donor densities contributes little to the measured capacitance and thus Mott-Schottky analysis in this linear region is invalid. On the contrary, in the linear region below the inflection, the C_{SC}^{-2} values increase with increasing applied potential due to the increased thickness of the electron depletion region, which is consistent with the assumption that the entire barrier layer is occupied by the depletion region [42]. Hence, the linear relation between C_{SC}^{-2} and applied potential in this region is related to the donor concentration of the passive films when fitted with Eq.(4).

The donor densities (N_D) and flatband potential (E_{fb}) values can be calculated by the slope and the intercept on the horizontal axis, respectively, using the linear fit of the C_{SC}^{-2} versus E plots. According to the XPS results, the values of dielectric constant, ε_r, are 45 (for Nb_2O_5 [43]) and 60 (for TiO_2 [44]) for the passive films grown on the NbN coating and the uncoated substrate, respectively. The calculated results for N_D and E_{fb} are listed in Table 4 and the values of N_D as a function of film formation potential are plotted in the inset of Fig. 8. Clearly, N_D values for both the coated and bare Ti-6Al-4V samples decrease with increasing film formation potentials, since the higher film formation potential is beneficial to the formation of a less defective and more ordered passive film. At the same film formation potential and cavitation exposure time, the calculated N_D value of the NbN coating is 1 ~ 2 orders of magnitude lower than that for bare Ti-6Al-4V. At a given film formation potential, when the cavitation exposure time increases from 0 h to 15 h, the N_D values for uncoated Ti-6Al-4V increase by an order of magnitude, whereas only a slight rise in the N_D values is observed for the NbN coating. Usually, the presence of oxygen vacancies serves as the charge carrier, and then the lower N_D value will lead to lower conductivity and electron transport, thereby slowing down electrochemical reactions [45]. Moreover, under the action of an electric field, the negatively charged chloride ions are preferentially absorbed into oxygen vacancy sites in these passive films and then the autocatalytic generation of cation vacancies proceeds. A rise in the concentration of cation vacancies facilitates migration of metallic cations and thus enhances the dissolution rate of the passive films, reducing the stability of the passive films. As a result, after different cavitation exposure times, the passive film grown on the eroded NbN coating is less likely to undergo localized corrosion in a containing Cl^- solution as compared with that present on the eroded uncoated Ti-6Al-4V. As can be seen from Table 4, the E_{fb} values for both the coated and uncoated Ti-6Al-4V samples shift towards more positive potentials with increasing cavitation exposure times and film formation potential. At the same film formation potential and cavitation exposure time, the E_{fb} values of the NbN coating are lower than that of bare Ti-6Al-4V. In general, a material with a less noble E_{fb} is less vulnerable to reacting with the anions present in the medium and hence has higher pitting resistance [46]. Therefore, after different cavitation exposure times, the NbN coating possesses a lower donor density and also indicates low reactivity with Cl^-, thereby enhancing the corrosion resistance of the Ti-6Al-4V coated with NbN. The results are consistent with the lower i_{corr} and higher impedance resistance for the coating as observed in the potentiodynamic polarization and EIS measurements.

For an n-type semiconductor, N_D decreases exponentially with increasing film formation potential (E_f) and the relationship between the N_D and E_f can be described using a first-order exponential decay function [47]:

$$N_D = \omega_1 exp(-bE_f) + \omega_2 \tag{5}$$

where E_f is the film formation potential, b is the decay constant, ω_1 and ω_2 are two unknown constants. The values of ω_1, ω_2 and b can be determined from the exponential fitting of N_D versus E_f data as shown in the insets of Fig. 8 to the Eq. (5). Considering that both niobium oxide and titanium oxide exhibit very high field strengths of the order of magnitude of $\sim 10^6$ V/cm, a high field approximation transport equation was employed to determine the diffusivity of oxygen vacancies (D_o) in the passive films grown on the tested samples [48]:

$$D_0 = \frac{z\alpha i_{ss}}{\omega_2 eExp(z\alpha\bar{\varepsilon}F/RT)} \tag{6}$$

where α is the half-jump distance of migrating point defects (assuming α = 0.25 nm), z is the charge number of the mobile point defects in the passive film, i_{ss} is the steady state current density in the passive film, e is the charge on an electron (1.6×10^{-19}C), F is the Faraday constant (94.485C/mol), R is the gas constant (8.314 J/K·mol), T is the absolute temperature (298 K), and $\bar{\varepsilon}$ is the mean electric field strength of the passive film. The steady-state thickness of the passive film (L_{ss}) can be estimated from the measured capacitance at the film formation potential and a frequency of 1 kHz using the equation [47]:

$$L_{ss} = \frac{\varepsilon\varepsilon_0}{C} \tag{7}$$

where ε is the dielectric constant of the passive film, ε_0 is the vacuum permittivity (8.854×10^{-14}F/cm), and C is the measured capacitance (μF/cm^2). The L_{ss} is related to E_f and $\bar{\varepsilon}$ as follows: [39]:

$$L_{ss} = \frac{1-\eta}{\varepsilon}E_f + B \tag{8}$$

where B is a constant and η is the polarizability of the passive film/solution interface. The value of η can be assumed to be 0.45 for a passive film under either steady-state or quasi-steady-state conditions [49]. The $\bar{\varepsilon}$ values can be determined from the linear fitting of L_{ss} and E_f by using Eq. (8). The calculated parameters, including D_o and L_{ss}, are listed in Table 4. According to the results listed in Table 4, with increasing cavitation exposure times, for both the coated and bareTi-6Al-4V samples show an increase in D_0 values, but uncoated Ti-6Al-4V has a more rapid rate of increase in the D_0 value. The results indicate that after the cavitation erosion tests, the passive films formed on the eroded samples exhibit a higher migration rate of oxygen vacancies than those formed under the quiescent electrolyte condition and the coating exhibits a higher self-healing ability than uncoated Ti-6Al-4V. At a given cavitation exposure time, the D_0 value for the eroded NbN coating was determined to be of the order of 10^{-16}cm^2/s and almost one order of magnitude less than that for eroded bare Ti-6Al-4V. Because the breakdown of the passive film is a diffusion-controlled process, the passive films formed on the eroded coating with a lower values of N_D and D_o provide a more efficient barrier to inhibit the mass transport of reaction ions. Further, at the same cavitation time, the L_{ss} value for the NbN coating is larger than that for uncoated Ti-6Al-4V, suggesting that the passive film present on the coating has less opportunity for dielectric breakdown.

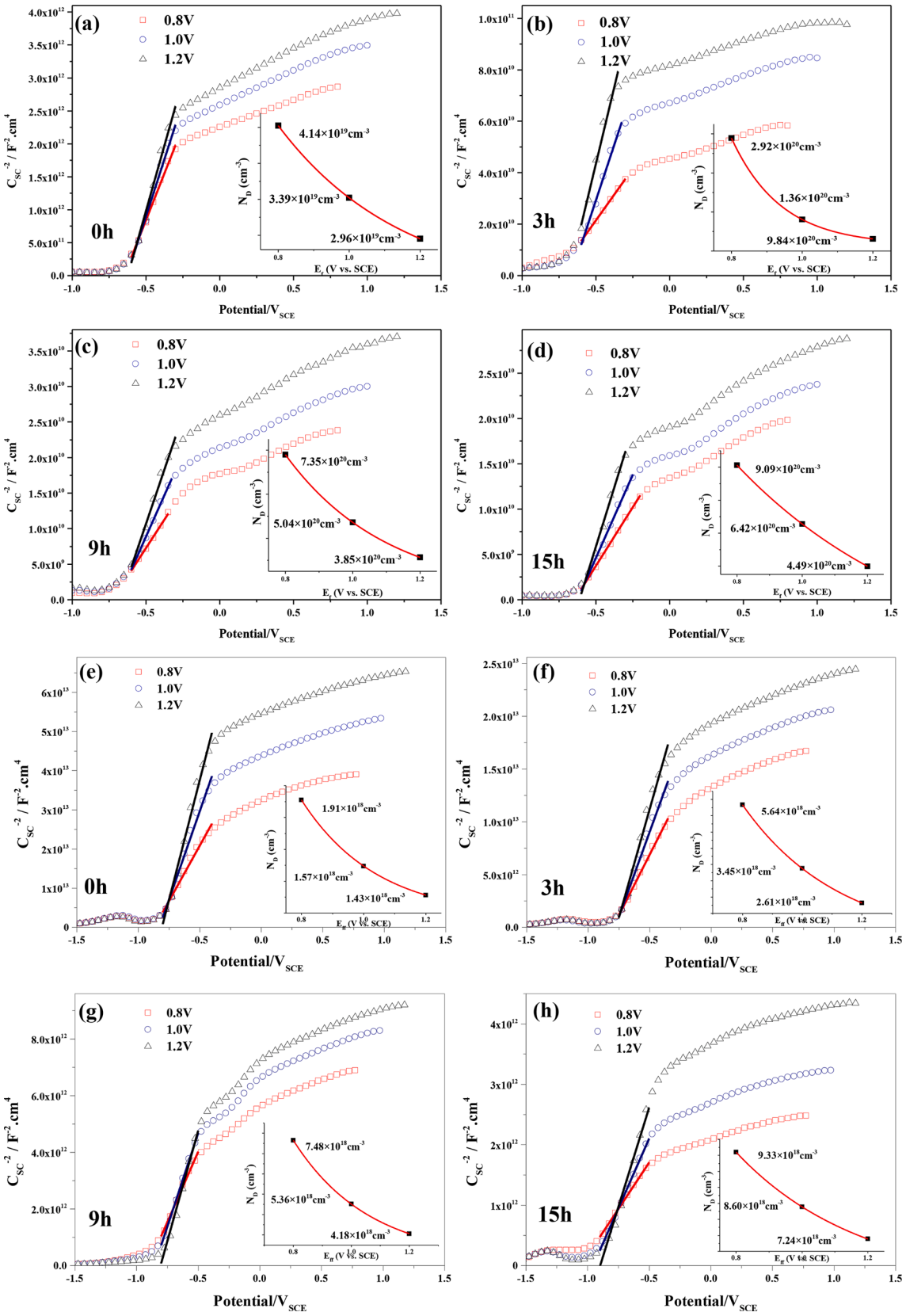

Fig. 8. Mott–Schottky plots of the passive films formed on (a-d) the uncoated Ti-6Al-4V and (e-h) the NbN coating before and after different cavitation erosion times in a 3.5 wt% NaCl solution. The illustration in each Mott–Schottky plot shows the donor density of the corresponding passive film at different film formation potentials.

Table 4
Electrochemical Parameters derived from capacitance measurement of the passive films formed on the NbN coating and uncoated Ti-6Al-4 V before and after different cavitation erosion times in a 3.5 wt% NaCl solution.

	Cavitation erosion time (h)	NbN coating				Uncoated Ti-6Al-4V			
		0 h	3 h	9 h	15 h	0 h	3 h	9 h	15 h
0.6V_{SCE}	N_D ($\times10^{19}cm^{-3}$)	0.19	0.56	0.75	0. 93	4.14	29.20	73.50	90.90
	E_{fb} (V)	−1.03	−0.91	−0.85	−0.8	−0.75	−0.73	−0.65	−0.64
	L_{SS}(nm)	5.13	5.73	8.88	19.4	9.23	18.33	23.51	36.58
0.8 V_{SCE}	N_D ($\times10^{19}cm^{-3}$)	0.16	0.35	0.54	0. 86	3.39	13.60	50.40	64.20
	E_{fb} (V)	−0.93	−0.85	−0.83	−0.78	−0.71	−0.69	−0.63	−0.63
	L_{SS}(nm)	5.61	6.39	10.81	21.34	10.17	18.94	27.43	39.58
1.2 V_{SCE}	N_D ($\times10^{19}$ cm^{-3})	0.14	0.26	0.42	0.72	2.96	9.84	38.50	44.90
	E_{fb} (V)	−0.89	−0.80	−0.81	−0.76	−0.68	−0.67	−0.62	−0.61
	L_{SS}(nm)	6.23	7.12	11.92	22.87	11.35	19.74	30.61	43.09
ω_2	9.21×10^{18}	1.02×10^{19}	1.44×10^{19}	1.76×10^{19}	1.16×10^{19}	2.43×10^{19}	4.57×10^{19}	5.79×10^{19}	
$\bar{\varepsilon}$(V/m)	6.68×10^{7}	5.12×10^{7}	3.79×10^{7}	2.63×10^{7}	1.41×10^{7}	1.13×10^{7}	9.79×10^{6}	8.16×10^{6}	
i_{ss} (A/cm^{-3})	4.36×10^{-8}	8.89×10^{-8}	1.21×10^{-7}	1.91×10^{-7}	8.32×10^{-7}	2.12×10^{-6}	4.72×10^{-6}	7.57×10^{-6}	
D_0 (cm^2 s^{-1})	4.07×10^{-16}	4.29×10^{-16}	5.72×10^{-16}	8.10×10^{-16}	9.52×10^{-16}	4.00×10^{-15}	7.34×10^{-15}	1.67×10^{-14}	

3.6. PZC measurements

To further evaluate the adsorption ability of chloride ions for the NbN coating after different cavitation exposure times, the point of zero charge (PZC) potential, which is defined as the electrode potential corresponding to a net zero charge at the sample/solution interface, was measured in a 3.5 wt% NaCl solution. Fig. 9 shows double-layer capacities of the tested samples as a function of applied potential in a 3.5 wt% NaCl solution, together with the E_{corr} for each sample represented by vertical lines. As shown in Fig. 9, each C_{dl}-E plot shows a minimum C_{dl} value, which corresponds to a potential defined as the E_{PZC} based on the Gouy-Chapman theory [50]. The potential differences between E_{corr} and E_{PZC} ($\Delta E = E_{corr}$ - E_{PZC}) is regarded as an indicator to judge the adsorbable type and number of ions on the sample surface [51]. If ΔE greater than 0, the sample surface is positively charged at E_{corr} and then readily adsorbs anions. On the other hand, if ΔE less than 0, the surface is negatively charged at E_{corr} and then is expected to repel anions. From Fig. 9, all the ΔE values of the tested samples are less than zero, implying that both the coated and bare Ti-6Al-4V samples repel Cl^- ions around their surfaces. With the increase of cavitation exposure time, the ΔE values of the tested samples decrease, indicating a decreased capability to repel Cl^- ions, and at a given cavitation exposure time, the NbN coating has a larger ΔE value and thus a stronger capability to repel aggressive Cl^- ions as compared to the uncoated substrate.

3.7. First-principles calculations

To further disclose the difference in donor density and the adsorption ability of chloride ions for the passive films present on the coated and uncoated samples, the formation energies of oxygen vacancies and the adsorption energies of Cl^- ions on the surface of the passive films grown on the two tested samples were calculated based on first-principles methods. In this work, rutile TiO_2 and B-Nb_2O_5 were selected to build the surface models of the passive films formed on the NbN coating and bare Ti-6Al-4V, respectively, due to their better thermal stability at ambient temperature as compared to other crystalline structures of TiO_2 and Nb_2O_5 [52,53]. The equilibrium crystal parameters of bulk rutile TiO_2 and B-Nb_2O_5 were first optimized to assess the reliability of the employed computational settings. As listed in Table S1 in the Supplemental material, discrepancies of the optimized lattice constants for the two compounds are less than 1% deviated from the available experimental data reported by others [54,55], suggesting that the computational parameters used here are reasonable. Because the rutile TiO_2 (1 1 0) and B-Nb_2O_5 (0 1 0) surfaces are the thermodynamically most stable crystal faces for these compounds, they were chosen as the surface models for the passive films [56]. As indicated in Fig. S7, two types of oxygen vacancy defects (that is, bridging oxygen vacancy (OB) and top oxygen vacancy (OT)) can be observed for the rutile TiO_2 surface model, whereas two types of oxygen vacancy defects (that is, two-fold (O_{2C}) and three-fold (O_{3C}) coordinated positions can be observed on the B-Nb_2O_5 surface model. Two types of defective rutile TiO_2 surface models and two types of defective B-Nb_2O_5 surface models with oxygen vacancies can be established through removing one oxygen atom from these coordinated positions, respectively, as shown in Fig. 10. The formation energies of different oxygen vacancies can be calculated by the following equation [57]:

$$E_{from}(V_O) = E_{tot}(\mathrm{def}) - E_{tot}(\mathrm{perfect}) + 1/2\mu(O_2) \quad (12)$$

where $E_{form}(V_o)$ is the formation energy of one oxygen vacancy, E_{tot}(def) is the total energy of the defective surface model, E_{tot}(perfect) is the total energy of the perfect surface model, and $\mu(O_2)$ represents the total energy of a molecular oxygen [58]. From the calculated results presented in Fig. 10, rutile TiO_2 has a smaller energy of formation for an oxygen vacancy than B-Nb_2O_5, indicating that oxygen atoms can more readily escape from the surface of rutile TiO_2. Therefore, compared with the B-Nb_2O_5, rutile TiO_2 has a higher oxygen vacancy concentration, which explains why the passive film formed on bare Ti-6Al-4V exhibits a larger N_D value.

Owing to the strong binding ability between oxygen vacancies and chloride ions, chloride ions tend to occupy the oxygen vacancies sites. To calculate the adsorption energy of chloride ions for rutile TiO_2 and B-Nb_2O_5, four possible adsorption models with one chloride ion located on adsorption sites that are the same as oxygen vacancy sites mentioned above, were constructed, as shown in Fig. 11. The adsorption energy of one chloride ion (E_{ads}) is given by [59]:

$$E_{ads} = E_{tot}(\mathrm{ads}) - E_{tot}(\mathrm{def}) - \frac{\mu}{2}(Cl_2) \quad (13)$$

where E_{tot}(ads) is the total energy of adsorption system, E_{tot}(def) is the total energy of the oxygen-deficient system, and $\mu(Cl_2)$ is the total energy for molecular Cl_2. As can be seen from Fig. 11, the adsorption energies of the four possible adsorption models are all negative, suggesting that the adsorption process of chloride ions can occur spontaneously. Compared with B-Nb_2O_5, rutile TiO_2 has more negative adsorption energies values, suggesting that rutile TiO_2 exhibits a stronger adsorption capability to the Cl^- ions than the B-Nb_2O_5. This agrees well with the results obtained from the PZC measurements.

4. Conclusions

In this investigation, a NbN nanoceramic coating was deposited on a Ti-6Al-4V substrate to enhance its cavitation erosion resistance. The nanoceramic coating consists of 13 μm thick δ′-NbN top layer and 2 μm thick (Ti, Nb)N diffusion interlayer. The coating not only exhibits higher

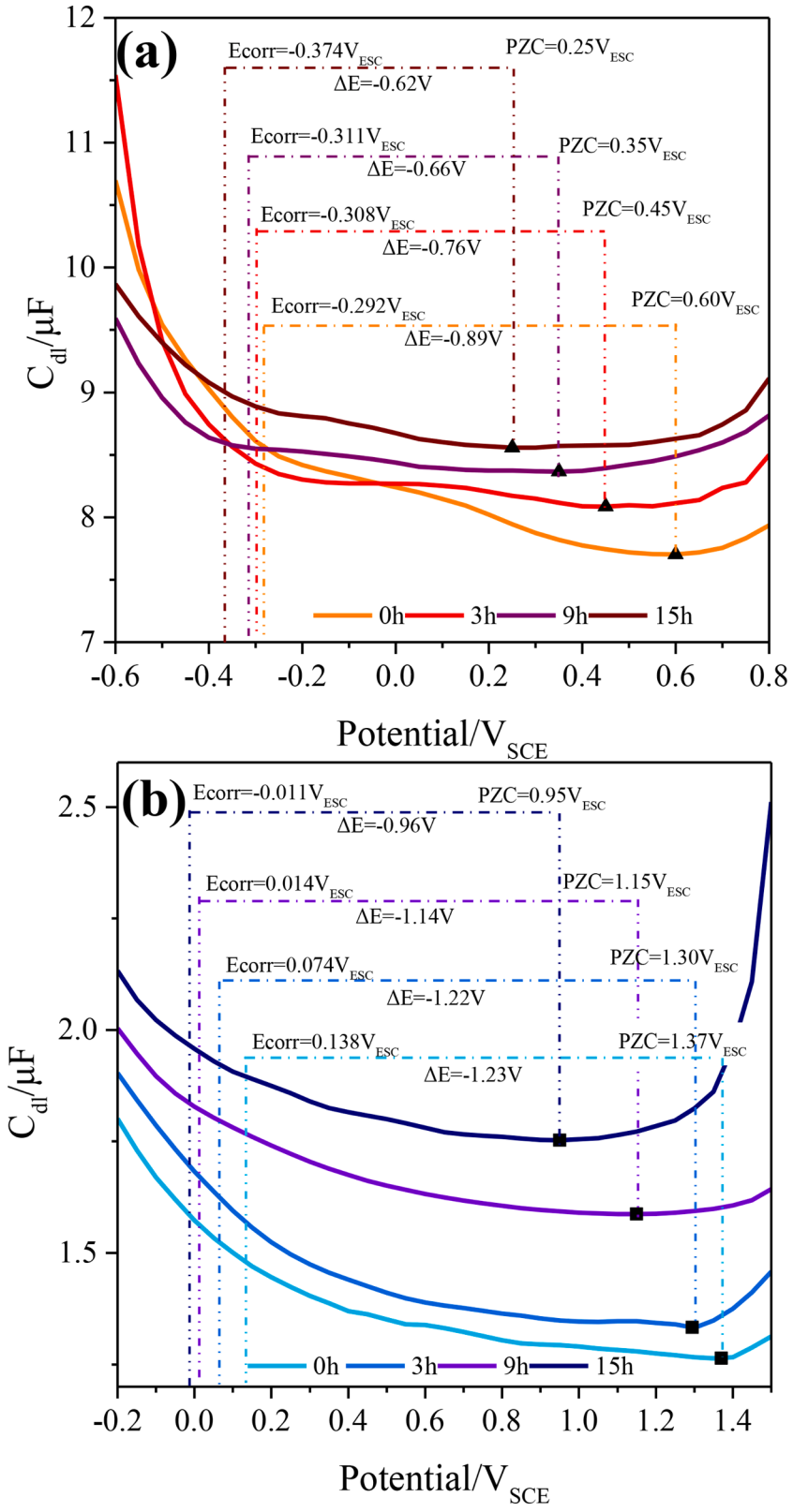

Fig. 9. Double layer capacities as a function of the applied potential for (a) the Ti-6Al-4V substrate and (b) the NbN coatings before and after cavitation erosion times of 3 h, 9 h and 15 h at an output power of 800 W in a 3.5 wt% NaCl solution.

contact damage resistance to localized attack induced by stress pulses, but the (Ti,Nb)N layer also offers a smooth transition in mechanical properties from the hard coating to the softer substrate. Electrochemical polarization measurements indicate that at a given cavitation time, the E_{corr} value of the NbN coating is nobler than that of uncoated Ti-6Al-4V, and its i_{corr} value decreased by two orders of magnitude as compared to that of uncoated Ti–6Al–4V. EIS measurements indicate that the impedance values of the NbN coating decrease with increasing

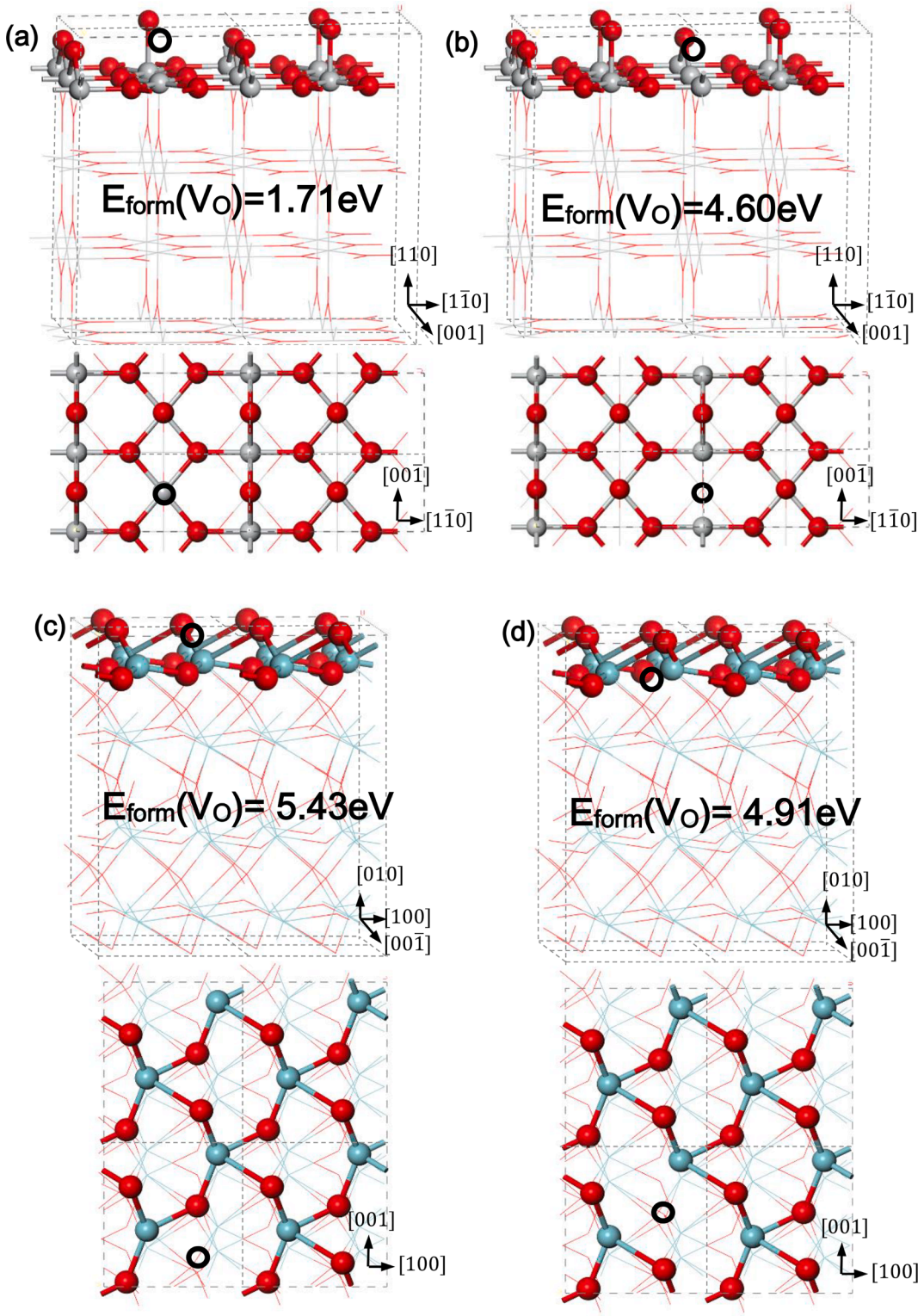

Fig. 10. Calculated structures (side and top views, respectively) of an isolated O vacancy at (a and b) the rutile TiO_2 (1 1 0)-2 × 2 surface and (c and d) the B-Nb_2O_5 (0 1 0)-2 × 2 surface formed through removing the oxygen atom (i.e. O_T, O_B, O_{2C} and O_{3C}) in (a), (b), (c) and (d), respectively. The circles illustrate the approximate positions of the isolated oxygen vacancies.

cavitation exposure time, and at a given cavitation erosion time, the impedance value of the NbN coating is significantly greater than that for bare Ti–6Al–4V. Mott-Schottky analysis indicates that the passive film grown on the NbN coating after different cavitation exposure times are characteristic of n-type semiconductor behavior, and at the same film formation potential and cavitation exposure time, the calculated N_D value of the NbN coating is 1 ~ 2 orders of magnitude less than that of uncoated Ti-6Al-4V. At a given cavitation exposure time, the diffusivity of oxygen vacancies (D_o) for the coating is of the order of $10^{-16}cm^2/s$ and almost one order of magnitude less than that for uncoated Ti-6Al-4V. PZC measurements show that the NbN coating has a stronger capability to repel aggressive Cl^- as compared to uncoated Ti-6Al-4V.

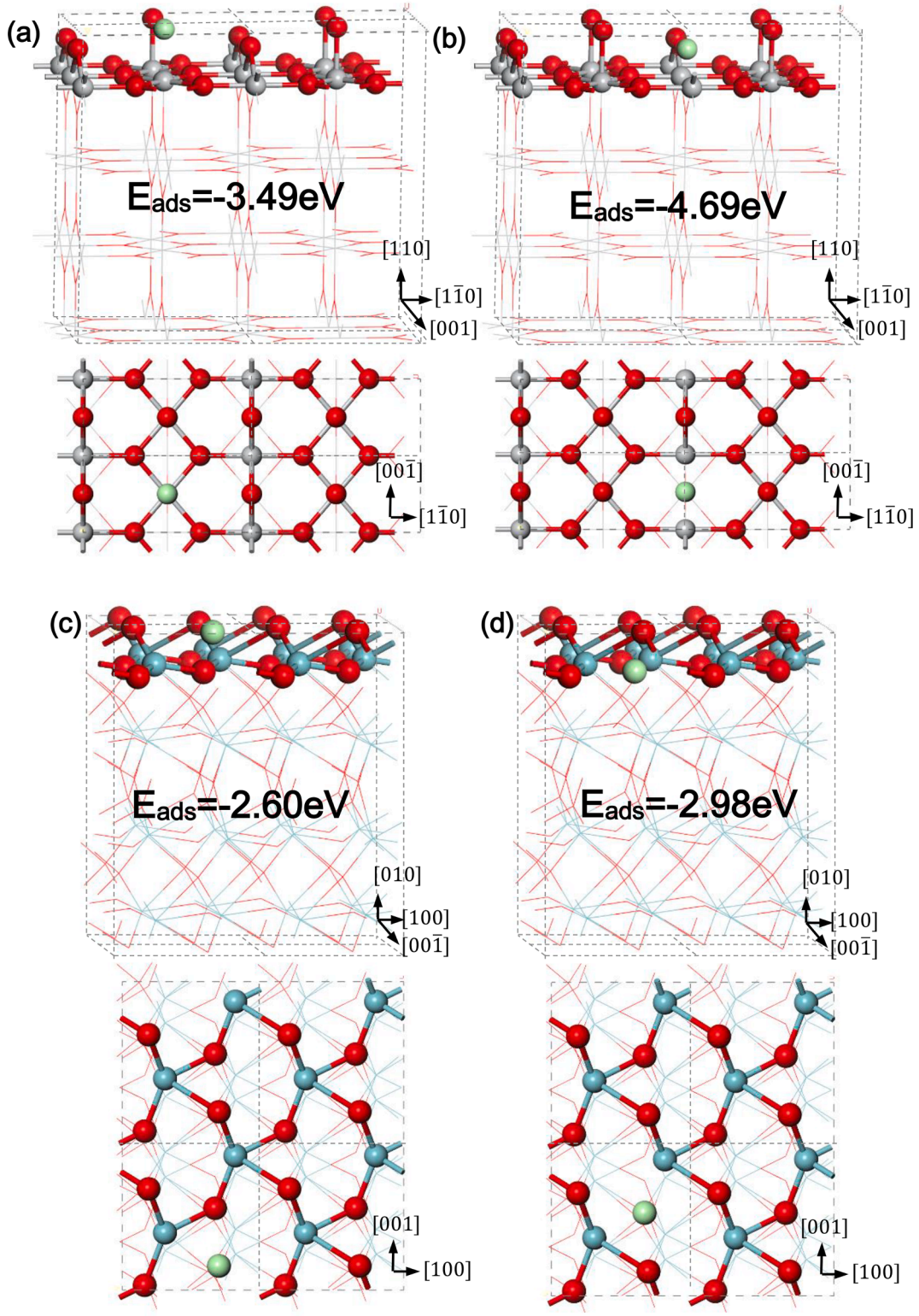

Fig. 11. Side and top views (upper and lower parts, respectively) of the calculated structures for a single Cl^- ion adsorbed on the oxygen vacancy site of the rutile TiO_2 (1 1 0)-2 × 2 surface and the B-Nb_2O_5 (0 1 0)-2 × 2 surface. The oxygen vacancy sites occupied by the Cl^- ion in (a), (b), (c) and (d) correspond to the oxygen atoms O_T and O_B on the rutile TiO_2 (1 1 0)-2 × 2 surface and O_{2C} and O_{3C} on the B-Nb_2O_5 (01)-2 × 2 surface respectively.

The formation energy of oxygen vacancies and the adsorption energies of Cl^- ions on the passive film on the coating were determined based on first-principles methods. The calculation results agree well with the data obtained from Mott-Schottky analysis and PZC measurements.

CRediT authorship contribution statement

Jiang Xu: Data curation, Writing - original draft. **Shuang Peng:** Investigation. **Zhengyang Li:** Conceptualization, Methodology, Software. **Shuyun Jiang:** Writing - review & editing. **Zong-Han Xie:**

Supervision. **Paul Munroe:** Writing - review & editing.

Declaration of Competing Interest

The authors declare that they have no known competing financial interests or personal relationships that could have appeared to influence the work reported in this paper.

Acknowledgements

The authors acknowledge the financial support of the General Program of the National Natural Science Foundation of China under Grant No. 52075245 and the Key Program of the National Natural Science Foundation of China under Grant No. 51635004.

Appendix A. Supplementary data

Supplementary data to this article can be found online at https://doi.org/10.1016/j.ultsonch.2020.105406.

References

[1] I.C. Park, S.J. Kim, Appl. Surf. Sci. 477 (2019) 37–43.
[2] F. da S. Severo, C.J. Scheuer, R.P. Cardoso, S.F. Brunatto, Wear 428 (2019) 162-166.
[3] A. Krella, Surf. Coat. Technol. 204 (2009) 263–270.
[4] Q. Luo, Q. Zhang, Z. Qin, Z. Wu, B. Shen, L. Liu, W. Hu, J. Alloys Compd. 747 (2018) 861–868.
[5] H. Li, Z. Cui, Z. Li, S. Zhu, X. Yang, Surf. Coat. Technol. 221 (2013) 29–36.
[6] Z. Ke Song, H. Herman, Wear 80 (1982) 101–113.
[7] A. Krella, A. Czyzniewski, Wear 266 (2009) 800–809.
[8] A. Krella, Wear 270 (2011) 252–257.
[9] A. Krella, A. Czyzniewski, Wear 265 (2008) 963–970.
[10] J. Xu, W. Hu, Z.H. Xie, P. Munroe, Surf. Coat. Technol. 296 (2016) 171–184.
[11] J. Xu, L. Liu, Z.H. Xie, P. Munroe, Surf. Coat. Technol. 206 (2012) 4156–4165.
[12] J. Xu, W. Liu, S. Jiang, P. Munroe, Z.H. Xie, Ultrason. Sonochem. 50 (2019) 138–156.
[13] J. Xu, S.K. Zhang, X.L. Lu, S. Jiang, P. Munroe, Z.H. Xie, Ultrason. Sonochem. 59 (2019) 104742–104761.
[14] A. Pogrebnjak, K. Smyrnova, O. Bondar, Coat. 9 (2019) 155–182.
[15] M. Benkahoul, E. Martinez, A. Karimi, R. Sanjinés, F. Lévy, Surf. Coat. Technol. 180–181 (2004) 178–183.
[16] K. Singh, A.C. Bidaye, A.K. Suri, Vacuum 86 (2011) 267–274.
[17] H. Shen, B. Wei, D. Zhang, Z. Qi, Z. Wang, Mater. Lett. 229 (2018) 17–20.
[18] L.X. Wang, J.C. Sun, J. Sun, Y. Lv, S. Li, S.J. Ji, Z.S. Wen, J. Power Sources 199 (2012) 195–200.
[19] M. Yang, A.J. Allen, M.T. Nguyen, W.T. Ralston, M.J. MacLeod, F.J. DiSalvo, J. Solid State Chem. 205 (2013) 49–56.
[20] W.C. Oliver, G.M. Pharr, J. Mater. Res. 7 (2011) 1564–1583.
[21] W. Du, L. Zhang, F. Ye, X. Ni, J. Lin, Physica B 405 (2010) 1695–1700.
[22] D. Vanderbilt, Phys. Rev. B 41 (1990) 7892–7895.
[23] J.D. Pack, H.J. Monkhorst, Phys. Rev. B 16 (1977) 1748–1749.
[24] M. Wen, C.Q. Hu, C. Wang, T. An, Y.D. Su, Q.N. Meng, W.T. Zheng, J. Appl. Phys. 104 (2008), 023527.
[25] K. Singh, A.C. Bidaye, A.K. Suri, Int. J. Corros. 2011 (2011) 267–274.
[26] A.H. Farha, A.O. Er, Y. Ufuktepe, G. Myneni, H.E. Elsayed-Ali, Appl. Surf. Sci. 258 (2011) 1613–1618.
[27] H.E. Cheng, M.H. Hon, J. Appl. Phys. 79 (1996) 8047–8053.
[28] S. Li, J. Deng, X. Qin, C. Ji, Surf. Eng. 33 (2017) 578–584.
[29] K.S. Havey, J.S. Zabinski, S.D. Walck, Thin Solid Films 303 (1997) 238–245.
[30] C.S. Sandu, M. Benkahoul, M. Parlinska-Wojtan, R. Sanjinés, F. Lévy, Surf. Coat. Technol. 200 (2006) 6544–6548.
[31] Z.H. Han, X.P. Hu, J.W. Tian, G.Y. Li, M.Y. Gu, Surf. Coat. Technol. 179 (2004) 188–192.
[32] M.A. Mamun, A.H. Farha, A.O. Er, Y. Ufuktepe, D. Gu, H.E. Elsayed-Ali, A. A. Elmustafa, Appl. Surf. Sci. 258 (2012) 4308–4313.
[33] S. Hogmark, S. Jacobson, M. Larsson, Wear 246 (2000) 20–33.
[34] S. Hong, Y. Wu, J. Zhang, Y. Zheng, Y. Qin, J. Lin, Ultrason. Sonochem. 27 (2015) 374–378.
[35] H.R. Bakhshandeh, S.R. Allahkaram, A.H. Zabihi, Ultrason. Sonochem. 56 (2019) 229–239.
[36] A. Darlinski, J. Halbritter, Z. Fresen, Anal. Chem. 329 (1987) 266–271.
[37] A. Ermolieff, P. Bernard, J. Less-Common Met. 120 (1986) 9–20.
[38] D.G. Li, D.R. Chen, P. Liang, Ultrason. Sonochem. 35 (2017) 375–381.
[39] R.M. Fernandez-Domene, E. Blasco-Tamarit, D.M. Garcia-Garcia, J. Garcia-Anton, Electrochim. Acta 95 (2013) 1–11.
[40] M. Schneider, S. Schroth, J. Schilm, A. Michaelis, Electrochim. Acta 54 (2009) 2663–2671.
[41] V.D. Jović, B.M. Jović, Corros. Sci. 50 (2008) 3063–3069.
[42] A.M. Schmidt, D.S. Azambuja, E.M.A. Martini, Corros. Sci. 48 (2006) 2901–2912.
[43] H. Habazaki, T. Matsuo, H. Konno, K. Shimizu, K. Matsumoto, K. Takayama, Y. Oda, P. Skeldon, G.E. Thompson, Surf. Interface Anal. 35 (2003) 618–622.
[44] D.G. Li, J.D. Wang, D.R. Chen, P. Liang, Ultrason. Sonochem. 29 (2016) 48–54.
[45] D.G. Li, J.D. Wang, D.R. Chen, P. Liang, Ultrason. Sonochem. 29 (2016) 279–287.
[46] S.P. Harrington, T.M. Devine, J. Electrochem. Soc. 156 (2009) 154–159.
[47] W. Wang, A. Alfantazi, Electrochim. Acta 131 (2014) 79–88.
[48] M. Bojinov, Electrochim. Acta 42 (1997) 3489–3498.
[49] D.S. Kong, J.X. Wu, J. Electrochem. Soc. 155 (2008) 32–40.
[50] S. Gao, C. Dong, X. Cheng, K. Xiao, L. Wang, X. Li, Corrosion 70 (2014) 627–635.
[51] Y. Liu, G.Z. Meng, Y.F. Cheng, Electrochim. Acta 54 (2009) 4155–4163.
[52] S. Perez-Walton, C. Valencia-Balvin, G.M. Dalpian, J.M. Osorio-Guillen, Phys. Status Solidi B 250 (2013) 1644–1650.
[53] Z.H. Cui, F. Wu, H. Jiang, Phys. Chem. Chem. Phys. 18 (2016) 29914–29922.
[54] S. Mezhenny, P. Maksymovych, T.L. Thompson, O. Diwald, D. Stahl, S.D. Walck, J. T. Yates, Chem. Phys. Lett. 369 (2003) 152–158.
[55] M.B. Pinto, A.L. Soares, A.M. Orellana, H.A. Duarte, H.A. De Abreu, J. Phys. Chem. A 121 (2017) 2399–2409.
[56] M.B. Pinto, A.L. Soares, M.C. Quintao, H.A. Duarte, H.A. De Abreu, J. Phys. Chem. C 122 (2018) 6618–6628.
[57] S.G. Wang, X.D. Wen, D.B. Cao, Y.W. Li, H.G. Wang, H.J. Jiao, Surf. Sci. 577 (2005) 69–76.
[58] P. Kowalski, B. Meyer, D. Marx, Phys. Rev. B 79 (2009) 115410–115417.
[59] Z. Luo, H. Zhu, T. Ying, D. Li, X. Zeng, Surf. Sci. 672–673 (2018) 68–74.